

# **Influence of Water Chemistry on Methylene Blue Adsorption by Hybrid Graphene Oxide-Cellulose Nanocrystal Sponges**

Raphaela Allgayer

Department of Chemical Engineering

McGill University, Montreal

November 2019

A thesis submitted to McGill University in partial fulfillment of the requirements of the degree of

**Master of Engineering in Chemical Engineering**



# Table of Contents

<b>1</b>	<b>Introduction</b>	<b>7</b>
<b>2</b>	<b>Theoretical Background</b>	<b>9</b>
2.1	Graphene and Graphene-Based Nanomaterials – Properties and Synthesis Methods	10
2.2	Graphene-Based Aquagels and Sponges	12
2.2.1	Thermodynamic Methods for 3DGS Synthesis	13
2.2.2	Self-assembly of GBNMs	14
2.3	Water Pollution Management with 3DGS	17
2.3.1	Adsorption Isotherms	18
2.3.2	Interaction Mechanisms between Organic Contaminants and GBNMs	19
2.3.3	Adsorption of MB and NOM on Activated Carbon and Carbon Nanomaterials	22
<b>3</b>	<b>Graphene Oxide Sponge as Adsorbent for Organic Contaminants: Comparison with Granular Activated Carbon and Influence of Water Chemistry</b>	<b>27</b>
3.1	Introduction	28
3.2	Materials and Methods	31
3.2.1	Preparation of rGO-CNC Sponges	31
3.2.2	Characterization of the Adsorbents	31
3.2.3	Adsorption Experiments	32
3.2.4	Quantification of MB and NOM	34
3.3	Results and Discussion	34
3.3.1	Material Characterization	34
3.3.2	Adsorption Studies	38
3.4	Conclusions	46
<b>4</b>	<b>Conclusions and Future Work</b>	<b>47</b>

## Acknowledgements

I would like to acknowledge the financial support of the Natural Sciences and Engineering Research Council of Canada; The Canadian Foundation for Innovation; and the Canada Research Chairs program. I would also like to thank CelluForce for providing the Cellulose Nanocrystals for this work, Dr. Jeffrey Farner and Andrew Golsztajn for their help with the HPLC method development, and Hemanshu Anand for his contribution in selected experiments.

On the other side of the Atlantic, I would like to acknowledge the financial support of the German Academic Scholarship Foundation (Studienstiftung des deutschen Volkes) and thank my family, friends, and Henri for all the rubber duck debugging, which they had to endure in the role of the rubber duck.

Most importantly, I would like to thank everybody in the Biocolloids and Surfaces Laboratory at McGill. All of you made my time in Montreal unforgettable. Special thanks to my office mates and the 12 am lunch group for insightful discussions, because great research happens where people with different backgrounds work together. I would also like to say a huge ‘thank you’ to Nathalie for opening up the door to research for me and for her guidance that extends way beyond the lab. It was an honor to work with all of you!

## Contribution of Authors

This thesis is submitted in accordance with the McGill University guidelines for manuscript-based theses. This document comprises four chapters: Chapter 1 sets the thesis into context; Chapter 2 reviews the literature and research objectives; Chapter 3 is a manuscript entitled 'Graphene Oxide Sponge as Adsorbent for Organic Contaminants: Comparison with Granular Activated Carbon and Influence of Water Chemistry'; and Chapter 4 contains a conclusion and recommendations for future work.

The manuscript that constitutes Chapter 3 is authored by Raphaela Allgayer, Nariman Yousefi, and Nathalie Tufenkji. To maintain consistency with the rest of this thesis, the orthography in this chapter has been corrected from the American standard used in the published manuscript. Design of experiments, most of the experimental work, data analysis and drafting of the manuscript were performed by Raphaela Allgayer. Nariman Yousefi characterized the materials, contributed valuable experience, drafted the sections regarding materials characterization and revised the manuscript. Nathalie Tufenkji provided valuable expertise and guidance throughout the project through her supervision, and participated in the revision of the manuscript.

## Abstract

In recent years, a number of nano-enabled technologies have been developed for water treatment applications. Among the most prominent are graphene oxide (GO) hydrogels or sponges. These porous graphene-based macrostructures combine the unique properties of the nanomaterial, namely an exceptional surface area, amphiphilic surface chemistry, and high mechanical strength, with the easy handling of a macroscopic bulk material. While the adsorption capacity of these adsorbents for a myriad of organic and inorganic compounds has been determined under controlled laboratory conditions, the effect of organic co-contaminants and water chemistry on the adsorption of target pollutants has often been omitted. Furthermore, GO sponges have only rarely been compared to the current industrial standard granular activated carbon (GAC).

This thesis evaluates a GO sponge under environmentally relevant conditions. By applying a simple HPLC-UV-vis method for the quantification of methylene blue (MB) in complex waters, we demonstrate that a reduced GO (rGO)-cellulose nanocrystal (CNC) sponge outperforms GAC in the removal of the model dye from single contaminant solutions and complex waters containing natural organic matter. Furthermore, the initial adsorption rate for MB is higher on the rGO-CNC sponge than on GAC. The difference in adsorptive performance is attributed to the surface chemistries and morphologies of the adsorbents. Lastly, adsorption on the rGO-CNC sponge is only mildly affected by the pH and the ionic strength of the contaminant solution, which demonstrates the versatility of the novel adsorbent.

## Résumé

Ces dernières années, un certain nombre de technologies nano-activées ont été développées pour le traitement d'eau. Parmi celles-ci, les hydrogels (éponges) d'oxyde de graphène (OG) sont parmi les plus importantes. Ces macrostructures poreuses à base de graphène combinent les propriétés uniques du nanomatériau - une surface superficielle exceptionnelle, une chimie de surface amphiphile et une résistance mécanique élevée – avec une aise de manipulation d'un matériau macroscopique. Bien que la capacité d'adsorption de ces adsorbants pour une multitude de composés organiques et inorganiques ait été déterminée dans des conditions de laboratoire contrôlées, l'effet des co-contaminants organiques et de la chimie de l'eau sur l'adsorption des polluants cibles est souvent omis. De plus, les éponges OG n'ont que rarement été comparées au standard actuel, le charbon actif granulaire (CAG).

Cette thèse évalue une éponge OG en conditions pertinentes pour l'environnement. En appliquant une simple méthode CLHP-UV/vis pour la quantification du bleu de méthylène (BM) dans des eaux complexes, cette thèse démontre ensuite qu'une éponge d'OG réduit (OGr) et de cellulose nanocristalline (CNC) surpasse la capacité du CAG à éliminer le colorant modèle de solutions à contaminant unique ainsi que d'eaux complexes contenant des matières organiques naturelles. De plus, le taux d'adsorption initial de BM est plus élevé pour l'éponge OGr-CNC que pour le CAG. La différence est attribuée aux chimies de surface et aux morphologies des adsorbants. Enfin, l'adsorption sur l'éponge OGr-CNC n'est que faiblement affectée par le pH et la force ionique de la solution, ce qui démontre la polyvalence du nouvel adsorbant.

# 1 Introduction

The field of Environmental Nanotechnology, which encompasses both the use of nanomaterials for environmental applications and the fate and transport of nanomaterials in the environment, became increasingly important with the large-scale production and use of nanomaterials in common consumer products, such as quantum dots in displays [4, 5] or titanium dioxide particles in sunscreen [6]. While the fate of nanoparticles upon (uncontrolled) release needs to be studied to sustainably develop these novel technologies and control their environmental impact, other nano-enabled technologies specifically aim at improving air, water and soil quality. Nanoparticles can be used to catalytically degrade [7] and sorb [8] potentially hazardous compounds, as well as in environmental sensors [9], membranes [10] or filters [11]. Often, these nano-enabled environmental technologies are meant to (partially) replace previously existing non-nano technologies. With these developments, big picture questions, that can be categorized according to the life-cycle of the nano-enabled technology, arise:

- **Resources and Production:** Is the production of the nanomaterial technically scalable to supply a sufficient quantity to replace the existing technology or is the novel technology tailored for niche applications? Is a scale-up economical? Are the resources required for the production of the nanomaterial readily available in a sustainable manner (compared to a previously existing technology)? How much energy and supporting chemicals are consumed in the production of the nanomaterial?
- **Use and Re-Use:** Does the nano-enabled technology outperform the previously existing non-nano technology (efficiency, quality, quantity)? What are the limitations of the nano-enabled technology? How does the nano-enabled technology behave under realistic application conditions? How is the nanomaterial recovered and re-used? Are any nanoparticles released over the life span of the nano-enabled technology? If yes, how much and are they harmful to the environment?

- **End of Life:** What is the life-span of the nano-enabled technology (compared to a previously existing technology)? How can the nanomaterial be disposed of? Can the nanomaterial be recycled?

This thesis aims at answering these questions for a graphene-based adsorbent for water treatment applications that has previously been developed in our group [12]. The questions regarding the synthesis of the nanomaterial and its assembly into a macroscopic adsorbent are discussed by reviewing the literature (Chapter 2). Then, Chapter 3 experimentally answers questions around the use of the adsorbent, its limitations and its comparison to the industrial standard adsorbent GAC. For the last group of questions, the end of life, reusability, environmental fate and transport, and ecotoxicity of the graphene-based adsorbent, the interested reader is referred to other scientific publications [13-15], as these questions extend beyond the scope of this thesis. The findings presented in the next chapters - the answers to a few of the questions above - and future work are summarized in Chapter 4.

## 2 Theoretical Background

Because of their large effective specific surface area [16] and their versatile chemistry [17, 18] that enables interaction with a myriad of water pollutants, graphene-based sponges have been identified as promising materials for water pollution management [19]. Resulting from their superior properties, these three-dimensional (3D) carbon nanosheet macrostructures outperform the common standard adsorbent granular activated carbon (GAC) in the adsorptive removal of many organic and inorganic contaminants from aqueous solutions [8, 20, 21]. While the adsorption of contaminants from single component solutions has been extensively studied, the effect of water chemistry is often neglected [8]. Furthermore, the sustainability of the material and its synthesis should be considered when discussing the use of graphene-based structures in environmental applications such as water treatment. Additionally, the novel material will only establish itself if its use is economical.

In the following, this section gives a brief overview of the synthesis of graphene and its derivatives (Chapter 2.1) as well as their assembly into macrostructures (Chapter 2.2). The processes are evaluated and compared considering environmental and economic aspects. Finally, Chapter 2.3 introduces the theory of molecular adsorption, explores potential interaction mechanisms between organic contaminants and graphene-based sponges and summarizes previous adsorption studies with the novel material.

## 2.1 Graphene and Graphene-Based Nanomaterials – Properties and Synthesis Methods

Graphene is a two-dimensional (2D) nanomaterial consisting of  $sp^2$ -hybridized carbon atoms that form a honeycombed lattice [22]. Due to its large system of delocalized electrons and the planar arrangement of its carbon atoms, the nanomaterial possesses exceptional physical and chemical properties, such as a very high surface area [23], super-hydrophobicity at nanometer scale [24], excellent electrical [24] and thermal [25] conductivity, and a high mechanical strength [26]. The combination of all these properties in one material makes graphene a promising candidate for various environmental applications, including desalination, air filtration and water pollution management [8].

Novoselov and Geim [24] first isolated single graphene layers through exfoliation of graphite. Since then, chemical vapor deposition (CVD) of hydrocarbons on transition-metal-carbide [27] or catalytic metal [28-30] surfaces followed by high cooling rates [30, 31] are used to synthesize pristine graphene for electrical applications. The resulting carbon monolayers are nearly free of defects, such that the extent of the delocalized aromatic  $\pi$ -electron system is maximized. However, for most environmental applications, larger quantities of graphene are needed, while the quality of the nanosheets is of less importance [16]. Additionally, the carbon films synthesized by CVD often show strong interactions with their substrate [28], which makes the isolation of the nanosheets challenging.

In the trade-off between quality and quantity, graphene for environmental applications is therefore often produced through exfoliation in a liquid, a method that yields more defective and impure nanosheets, but is also more scalable [3, 32]. Loyota [33] and Hernandez [34] use a non-polar organic solvent with similar surface energy as graphene to overcome the stacking energy of graphite [35]. Under ecological considerations, the extensive use of solvent in these processes is highly questionable. Hence, when possible, graphene is replaced by its derivatives graphene oxide (GO) or reduced graphene oxide (rGO). In these nanomaterials, the aromatic domains of the nanosheets are interrupted by epoxy, hydroxyl, carboxyl and carbonyl functional groups [18, 36]. Stankovich [1] suggested a general reaction scheme for the synthesis of GO and rGO from stacked graphene sheets, better known as graphite (Figure 1). As a first step, the interlayer spacing of

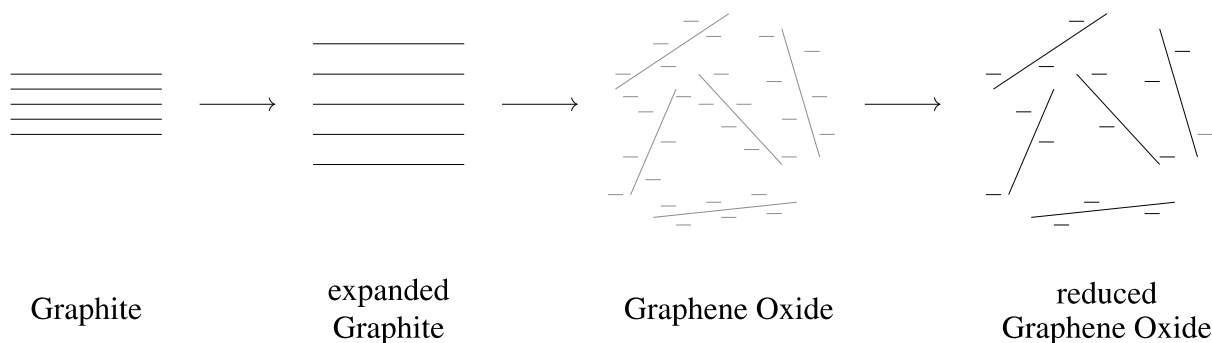


**Figure 1.** Synthesis of GO and rGO as suggested by Stankovich [1]. In the first step, the interlayer spacing of graphite (black) is thermally increased to form expanded graphite. Next, the expanded graphite is oxidized and suspended. Lastly, the GO sheets (gray) are reduced to a varying extent, such that rGO (black) is formed. Figure adapted from [3].

graphite is increased through thermal treatment, making the surfaces of the carbon sheets more accessible to small molecules. This enables the introduction of oxygen functional groups on both sides of the expanded graphite layers and on their edges, imposing a negative surface charge on the nanomaterial. Hence, the attractive inter-sheet forces dominant in graphite are outweighed by electrostatic repulsion, such that the GO nanosheets are easily dispersed in water upon stirring or sonication. Furthermore, the polar and charged functional groups on the GO sheets enhance the colloidal stability of the material, as they counteract hydrophobic effects that cause the agglomeration of pure graphene in polar liquids. The most frequently used oxidizing agents in the synthesis of GO from expanded graphite are potassium permanganate and sulfuric acid with or without nitric acid or phosphoric acid, as suggested by Hummers [37] and modified versions of his method [38, 39]. Less common procedures apply potassium chlorate and nitric acid to oxidize expanded graphite [40, 41].

To restore aromatic domains on the surface of the oxidized nanomaterial, thermal treatment [42, 43] and various reducing agents [44-46] have been applied. While thermal treatment is very energy intensive, most strong reducing agents, such as hydrazine [44], have severe consequences for the environment. Fernández-Merino and co-workers [45] showed that nontoxic L-ascorbic acid, better known as vitamin C (VC), exhibits a similar GO reduction efficiency as hydrazine. Depending on the application, milder reducing agents, such as tannic acid [47] or other phenolic acids [48], might also sufficiently reduce GO. While the delocalized  $\pi$ -electron system of the rGO formed under strong reductive conditions is mostly restored and the nanomaterial resembles graphene in its

chemical behavior [43], less reduced rGO still exhibits both polar and non-polar domains [21]. Therefore, the latter forms stable dispersions like GO, but strongly reduced rGO agglomerates because of hydrophobic effects and the lack of electrostatic repulsion [44].

Despite the inferior quality of rGO compared to graphene obtained by CVD or exfoliation and the use of strong oxidizing agents, the synthesis of rGO in aqueous conditions is the best compromise in terms of cost, scalability and sustainability known to this day. Especially when refraining from using nitric acid for the oxidation and applying environmentally friendly reducing agents, the required amount of toxic chemicals and energy consumption are minimized. Additionally, the process is fairly easily scalable and costs are comparably low.

## 2.2 Graphene-Based Aquagels and Sponges

Crucial to adsorption processes is the removal of the adsorbent from the treated fluid, as the release of the loaded adsorbent into the environment can be as harmful as the contaminant itself [15]. In the case of nanomaterials, the design of this process step is especially challenging. Because of their small size, the nanosheet movement in liquids is dominated by Brownian motion. Hence, the particles do not settle over time unless a strong centrifugal force is applied to the system. Alternatively, the removal of the particles through filtration is very energy intensive. To overcome this problem and to extend the application capabilities [49] of these nanomaterials, graphene and graphene-related nanomaterials (GBNMs) are assembled into 3D graphene-based macroscopic structures (3DGSs). Among this group of materials are so-called aquagels, which can be removed from the processed liquids in a simple liquid/solid separation step.

Aquagels are highly cross-linked colloids, which behave like solids, although their volumetric water content can be as high as 99.7 % [50]. While the term *hydrogel* encompasses gels whose network component can be either a polymer or colloidal network, *aquagel* only refers to structures consisting of nanoparticles and water [51]. When hydrogels are removed from their surrounding liquid, they collapse due to the surface tension of the liquid during drying. The resulting nanoparticle or polymer films are called *xerogels*. If the highly porous structure of a hydrogel is preserved in the dried state, the gel is classified as an *aerogel*. Methods that prevent surface tension-related forces from acting upon the network structure, such as (vacuum) freeze drying or critical

point drying [52] are used to convert hydrogels into aerogels. Likewise, an aerogel is converted into a hydrogel simply by immersion into water. However, aerogels in which polar nanoparticles are connected through non-chemical interactions might disintegrate upon exposure to water [16]. Aquagels are mostly prepared via self-assembly from colloidal dispersions, aerogels are generally synthesized through template directed growth and thermodynamic methods.

### 2.2.1 Thermodynamic Methods for 3DGS Synthesis

Freeze drying and unidirectional freeze drying of GO dispersions are two common thermodynamic synthesis methods for 3DGSs. Both processes rely on the sublimation of water from frozen colloidal GO to obtain lightweight aerogels with a monomodal pore size distribution and very thin pore walls [53]. The pore size of these structures depends mainly on the freeze-drying parameters super-cooling temperature and temperature gradient, as well as GO sheet size and concentration. While the pores in freeze dried aerogels resemble a random network, whose formation is driven by the arbitrary shape and orientation of the ice crystals in the frozen dispersion, unidirectional freeze drying creates an anisotropic material with parallel aligned pores [48]. The one-dimensional temperature gradient, which is applied to the colloid in unidirectional freeze drying, causes the formation of long, rod-shaped, parallelly arranged water crystals in the GO dispersion. As in common freeze drying, the ice structures then act as *in situ* developed soft templates for the aerogel synthesis, with the dispersed nanosheets forming a second GBNM-rich phase in the spaces between the water crystals. When the ice is removed, the GO is held together in this arrangement through weak physical interactions. In a subsequent step, 3DGSs obtained by freeze drying can be reduced by applying high temperatures [54] or hydrazine vapor [55] to ensure structural stability upon immersion of these GO-based aerogels into water.

In contrast, template directed growth of 3DGSs denotes the chemical synthesis of a porous material around a previously existing template. In most of these processes, nickel foam acts as a template and catalyst for CVD with ethanol, hexane, methane or ethane as a precursor [16]. In brief, the nickel substrate is exposed to a vaporous carbon source, which decomposes on its surface to form the honeycombed carbon lattice of graphene [28]. As soon as the nickel foam is well coated with graphene, it is etched away with 3 M hydrochloric acid [56, 57]. The result is a hydrophobic, ultra-

lightweight 3DGS with a monomodal pore size distribution. The pore size of these structures depends on the characteristics of the nickel foam template and the cooling rate of the freshly formed graphene foam, both of which can be easily adjusted to optimize the morphology of the 3DGS [58]. If a 3DGS obtained by CVD is meant to be used in an aqueous environment, it must be oxidized following its synthesis to overcome its hydrophobicity.

### 2.2.2 Self-assembly of GBNMs

Due to their immense energy consumption, sensitivity and instrumental effort, both thermodynamic synthesis and template directed growth of 3DGSs are hardly scalable enough to produce porous macrostructures for water remediation purposes. Consequently, the self-assembly of aquagels from stable colloids, also called sols, has been identified as promising method for the synthesis of 3DGS. While colloidal graphene and strongly reduced rGO dispersions are not stable in water, GO and more mildly reduced rGO dispersions can be classified as sols.

The DLVO theory [59, 60] describes the interaction between dispersed nanoparticles<sub>1</sub> to explain their colloidal stability. In brief, the model overlays the effects of van-der-Waals attraction with electrostatic repulsion to determine the overall potential of a particle as a function of distance from its surface (Figure 2). The resulting curve generally exhibits a maximum, the repulsive barrier, and two minima, which are referred to as primary and secondary minimum, respectively. Two particles in dispersion are reversibly attracted to each other until they reach the separation distance of the secondary minimum and form *flocculates*. If the potential energy of the local maximum is in the order of magnitude of the average thermal energy of the particles  $k_B T$ , the repulsive barrier can be overcome and the flocculates spontaneously ‘fall’ into the primary energy minimum, such that the

<sub>1</sub> GBNMs are considered nanoparticles, because they extend over 10 nm to 1000 nm in two dimensions [24]. However, due to their sheet-like structure, the third dimension of the nanomaterial measures only one to a few atoms, which is a characteristic dimension for molecules. Hence, the aggregation properties of GBNMs range between those of molecules and those of nanoparticles. For simplicity, this thesis explains the gelation of GBNMs by models applicable to nanomaterials. Nevertheless, the reader should keep in mind that some well-established models, e.g. the electric double layer, might not be applicable to GBNMs, because the interactions of the large surface of the sheets with ions might be governed by molecular mechanisms.

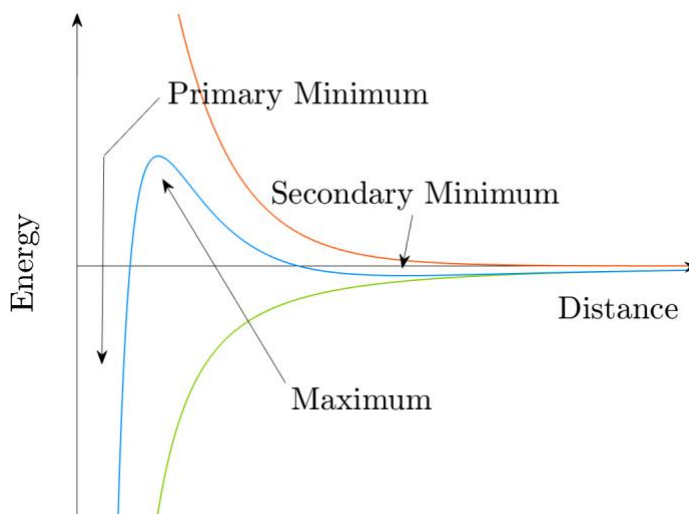


**Figure 2.** The DLVO theory describes the interaction energy between two particles in solution as a function of their distance from each other (blue). The characteristic extrema result from the addition of the van-der-Waals attraction between two particles (green; proportional to  $1/r^n$ ) and their electrostatic repulsion (orange, exponential decay).

particles are irreversibly agglomerated. However, if the repulsive barrier is greater than  $k_B T$ , the nanoparticles cannot put up the energy to *coagulate* and remain in the flocculated state. Nanoparticle dispersions which reversibly agglomerate, or flocculate, are called stable colloids or *sols*.

Upon addition of a gelling agent to highly concentrated sols, the particles form the porous network of a gel. Gelling agents can chemically modify the surface of the particles or act as crosslinkers between nanoparticles. When lowering the pH of a GO/rGO dispersion, the oxygen functional groups on either side of the sheets become protonated. As a result, the particles are less hydrated, their electrostatic repulsion is reduced and their interaction is governed by hydrophobic  $\pi - \pi$  and van-der-Waals forces, as well as hydrogen bonding between the oxygen functional groups [61]. While this chemical modification would cause small GO/rGO sheets to align in parallel and precipitate, larger GO/rGO sheets assemble into porous structures with randomly oriented sheets. Even in dilute dispersions, the motion of large GO/rGO sheets is limited by the surrounding nanoparticles. Thus, upon protonation of the oxygen functional groups, the sheets cannot arrange themselves in thermodynamically favorable parallel stacks, but remain in their random configuration [62].

The reduction of the oxygen containing surface groups on large GO/rGO, which restores the aromaticity of the nanosheets, is another mechanism that induces gelation of the nanomaterial through chemical alteration of the surface. After the removal of the oxygen functional groups, hydrophobic effects outweigh the electrostatic repulsion between the particles and the colloidal rGO gels spontaneously. Common reduction methods include high temperature and pressure [53, 63, 64] and the use of reducing agents [12, 42, 65]. In general, the chemical removal of the oxygen functional groups with strong reducing agents such as hydrazine, NaBH<sub>4</sub> or VC is more efficient than the hydrothermal method [16], yielding more aromatic and less hydrophilic sponges. However, the reduction of GO with highly toxic hydrazine or NaBH<sub>4</sub>, which reacts strongly with water, generates large quantities of gas that disrupt the gelation. In contrast, edible VC releases only water upon oxidation and is therefore the most convenient gelling agent from both an environmental and material engineering perspective [45].

Crosslinkers can be applied to chemically or physically connect the sheets. The addition of long chain-like molecules to colloidal GO/rGO increases its viscosity. Consequently, the reduced motion of the dispersed nanoparticles enables the formation of physical bonds between the functional groups of the gelling agent and the GO/rGO sheets [66]. Physical crosslinking materials include both synthetic [62, 67, 68] and natural [66, 69, 70] polymers. Alternatively, chemical crosslinkers can form complexes [61, 71] or covalent bonds [72, 73] with two or more GO/rGO sheets. Cong and co-workers [74] have synthesized a stretchable and self-healing GO-polymer composite material applying both chemical and physical crosslinkers. If the interaction mechanism between the crosslinker and GO/rGO involves electrostatic attraction between opposite (partial) charges, gelation induced by crosslinkers is pH sensitive [62]. Hydrogels synthesized with the aid of crosslinkers might be freeze dried and reduced to improve their hydrophobicity and electrical conductivity [75].

Besides facilitating their gelation, crosslinkers also enhance the strength and elasticity of GBNM gels. Especially for their application as adsorbents, 3DGSs should be mechanically stable while compromising the surface area of the dispersed nanosheets as little as possible. In general, 3DGSs with thicker pore walls, i.e. more layers of GBNM, are sturdier but also exhibit a lower specific surface area [76]. Gels or sponges, whose pore walls consist of more than a few layers of the nanomaterial, exhibit a lower fraction of graphene or graphene derivative sheets that is exposed to the inner pore walls and, therefore, ‘visible’ for the adsorbate. On the other hand, 3DGSs with a

high internal surface area and pore volume show a similar adsorption behavior as graphene, GO or rGO dispersions, but might break down under minor mechanical stress. Besides the crosslinkers discussed above, rod-shaped nanomaterials like carbon nanotubes (CNTs) [77] and cellulose nanocrystals (CNCs) [12] are incorporated in ultralight graphene structures as plasticizers, strengthening agents and spacers.

As an alternative to rod-shaped spacers, sacrificial templates can be built into 3DGSs during gelation to engineer the pore size of the so-formed aquagels. While the incorporation of spacers might alter the chemical and physical properties of 3DGSs through the introduction of new functional groups to the system, templates are removed from the aquagel after formation, leaving the pure GBNM behind. Sui and co-workers [78] applied VC as a template and reducing agent simultaneously. If the concentration of VC is above its solubility limit in the GO dispersion, the GO sheets assemble around the insoluble VC grains following their reduction by VC. By washing the aquagel with water, the VC is removed from the structure leaving a hierarchically porous 3DGS behind. The so-obtained aquagels exhibit a high specific surface area and good interconnectivity between the pores [8]. Alternatively, extensive re-stacking of GBNM sheets can be prevented through a regulated release of gaseous reduction products, as Zhao et al [53] and Niu et al [55] demonstrated by synthesizing of thiourea-reduced hydrothermally-gelled graphene sponges and hydrazine vapor-reduced hydrothermally gelled graphene foams, respectively. Among the myriad of self-assembly methods for 3DGSs, low temperature and pressure procedures consume significantly less energy than their hydrothermal counterparts. Hence, from an environmental perspective, the self-assembly through reduction by a non-toxic reducing agent such as VC is a promising method for the synthesis of 3DGSs for water treatment applications. Furthermore, spacers and crosslinkers should be chosen to be sustainable in their production and biodegradable when released into the environment.

## **2.3 Water Pollution Management with 3DGS**

Because of their exceptional available surface area, amphiphilic character and delocalized  $\pi$ -electron system, 3DGSs attract a wide range of anthropogenic and natural water contaminants [19].

Hence, sustainably produced 3DGSs are ideal candidates for the adsorptive removal of organic and inorganic compounds from water.

### 2.3.1 Adsorption Isotherms

*Adsorption* is a simple wastewater treatment strategy based on the increase in concentration of atoms, ions or molecules on the interface between a fluid and a solid phase [51]. The association of the dissolved (contaminant) species, also called *adsorbate*, and the solid phase, which is referred to as *adsorbent*, is governed by a combination of interaction mechanisms specific to the adsorbate-adsorbent system. Thus, various models have been introduced to facilitate the description of adsorption mechanisms and provide information about the sorption capacity of an adsorbent for a specific adsorbate.

Among the most common models is the Langmuir adsorption isotherm [79]. It is based on the assumptions that an adsorbent consists of distinct, energetically equivalent adsorption sites and that all adsorbate molecules are of the same species. Once an adsorption site is occupied, no other adsorbate can interact with this specific site. Hence, the adsorption capacity of an adsorbent is reached when all sites are occupied by one molecule and a monolayer of adsorbate molecules is formed on the solid surface. As the energetic state of an adsorption site is not influenced by the vacancy of the neighboring adsorption sites, i.e. there are not interactions between adsorbed molecules, the adsorption sites are filled up in a random order. Thus, according to Langmuir, adsorption is an equilibrium process, that can be described as a reversible reaction between an empty adsorption site  $S$  and an adsorbate molecule  $A$  to form an adsorbed adsorbate species  $A^*$



Considering all these simplifications, the Langmuir isotherm quantitatively describes equilibrium adsorption as

$$\frac{1}{q_e} = \frac{1}{b q^{max} c_e} + \frac{1}{q^{max}} , \quad (2)$$

where  $q_e$  is the mass of adsorbed adsorbate  $A^*$  at equilibrium divided by the mass of the adsorbent,  $b$  is a parameter related to the adsorption energy,  $c_e$  is the adsorbate concentration in the solution

at equilibrium and  $q_{max}$  is the maximum specific adsorption capacity of the adsorbent for adsorbate A.

The Langmuir adsorption isotherm falls short when the adsorbate surface is energetically inhomogeneous or when interactions between adsorbate molecules cannot be neglected. Freundlich's empirical adsorption model [80] allows for multilayer adsorption of one adsorbate species and heterogeneous adsorption sites. With  $K_F$  as an indicator for the adsorption capacity and  $n$  as an empirical parameter that is related to the affinity of the adsorbate to the adsorbent, the Freundlich isotherm is written as

$$q_e = K_F c_e^{1/n}. \quad (3)$$

Other single adsorbate isotherm models, such as the empirical Redlich-Peterson [81] or the Brunauer–Emmett–Teller isotherm [82], apply three fitting parameters to describe experimental adsorption measurements or are developed for the accumulation of an adsorbate on a gas-solid interface, respectively. Newer models account for multiple adsorbate species. However, these models are often restricted to species of the same molecular radius [83] or assume no interactions between the adsorbates [84], such that more complex systems cannot be sufficiently described with the existing models.

### **2.3.2 Interaction Mechanisms between Organic Contaminants and GBNMs**

The adsorption mechanism is governed by the chemical and physical interactions between adsorbate and adsorbent. If the adsorbate chemically reacts with the adsorbent, the enrichment of the dissolved species on the solid-fluid interface is classified as chemisorption. Physisorption is the weak (physical) interaction of the adsorbate with the adsorbent. Organic contaminants are attracted to 3DGSs mostly through weak interactions. The main exception is Lewis acid-base reactions, where the hydrogen of the oxygen functional groups of GO/rGO acts as an electron acceptor for an electron donating nitrogen functional group of the adsorbate [85]. A small group of organic contaminants also chemisorb to 3DGSs through covalent bonding with the oxygen functional groups.

However, most organic compounds physisorb to the adsorbent. In general, physical interactions can be classified as either polar or non-polar interactions, both of which are governed by (partial) charges. Polar interactions, occurring between two or more molecules with an inherent electronegativity difference between their atoms or charged molecules, include hydrogen bonding, dipole-dipole and electrostatic interactions. If two atoms in one molecule differ in their electronegativity, the electron distribution in the molecule is shifted towards the more electronegative atom and the molecule exhibits a so-called dipole. Two such molecules interact with each other through dipole-dipole interactions. If the very electronegative species oxygen, nitrogen, sulfur or the halogens, as well as their electropositive counterpart hydrogen participate in such an interaction, it is referred to as hydrogen bonding. Electrostatic forces act between two ions, i.e. molecules or atoms with at least one elementary charge<sup>2</sup>. In a special case of electrostatic interactions, the  $\pi$ -electron system of one molecule interacts with cations or protons, which is referred to as cation- $\pi$  or hydrogen- $\pi$  bonding, respectively [86].

All polar adsorption mechanisms depend strongly on the pH of the contaminant solution [87, 88]. At pH values below the point of zero charge of the adsorbent, the oxygen functional groups of GO/rGO are heavily protonated resulting in a positive surface charge [66, 89]. As the pH increases, the functional groups become less protonated, such that adsorbates interact with the adsorbent mostly through hydrogen bonding and dipole-dipole mechanisms. In these moderately acidic environments, the adsorption energy barrier through these mechanisms is relatively low, because the oxygen functional groups are only lightly hydrated. As the pH value increases further, hydrogen bonding gives way to electrostatic interactions between the adsorbate and the negatively charged adsorbent surface [66, 90]. However, at moderate to high pH values, the oxygen functional groups are also highly hydrated [47]. This imposes an activation energy on the adsorption of other ions, as the layer of water molecules around an ionic center has to be removed before the adsorbate can bind to the adsorbent. Small ions, such as sodium, reduce the interactions between adsorbent and

<sup>2</sup> Strictly speaking, electrostatic forces are also responsible for dipole-dipole interactions, hydrogen bonding and non-polar interaction mechanisms. However, for the better distinction between the adsorption mechanism of an ionic organic compound and a neutral organic compound, in this thesis, the term *electrostatic interaction* only refers to interactions between ions.

water, lowering the activation energy of the adsorption [91]. Hence, the adsorption of organic contaminants might increase with the ionic strength. Due to the different pK<sub>A</sub> values of the oxygen functional groups on GBNMs, multiple interaction mechanisms occur at the same time within one sponge. The solubility, hydration and charge of the adsorbate are also a function of the pH [20, 90, 92] and the ionic strength [91].

Non-polar interactions between an adsorbate and an adsorbent are less dependent on the pH of the surrounding solution. Besides van-der-Waals interactions that act between all molecules and particles in solution,  $\pi - \pi$  interactions are of special interest when GBNM surfaces are adsorbents for organic contaminants. Contrary to van-der-Waals interactions, which are mainly caused by electron cloud fluctuations in molecules made up of elements of the same electronegativity,  $\pi - \pi$  stacking can be traced back to the permanent unequal charge distribution within an aromatic structure (of equally electronegative carbon atoms). In molecules with a conjugated  $\pi$ -electron system, the electron probability density is higher above and below the planar sp<sup>2</sup>-hybridized carbon atoms. Hence, the carbon scaffold itself is slightly positively charged, while planes above and below the carbon structure exhibit a negative charge. When interacting with each other, these sandwich structures arrange themselves in a T-configuration or in an axis shifted planar stacking configuration (Figure 3). Concentric stacking only occurs between a molecule with an electron deprived aromatic structure and an aromatic structure with electron donating ligands.  $\pi - \pi$  interactions of GBNMs with aromatic adsorbates that contain electron withdrawing groups are stronger than those with regular or electron-rich conjugated structures [85].

The adsorption of an aromatic structure results from the combination of multiple interaction mechanisms [88]. While polar interactions occur mostly between the negatively charged functional groups of GBNMs and the adsorbate, the carbon scaffold of the adsorbent attracts adsorbates through non-polar interactions. Therefore, the removal of cationic contaminants is favored over the adsorption of neutral or anionic molecules on 3DGSs [19]. However, even negatively charged adsorbates can spontaneously adsorb to GO/rGO if the non-polar attractive interactions outweigh the electrostatic repulsion between the oxygen functional groups of GO/rGO and the anionic organic molecule [93].

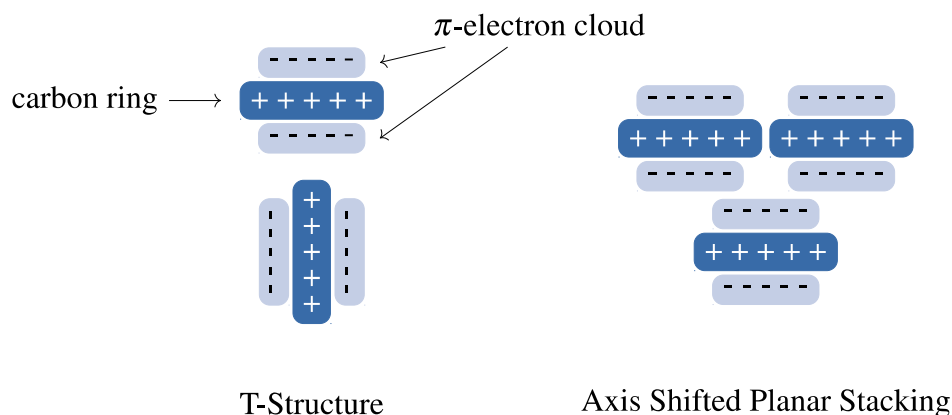


**Figure 3.**  $\pi - \pi$  stacking configurations T-structure (left) and axis shifted planar stacking (right).

### 2.3.3 Adsorption of MB and NOM on Activated Carbon and Carbon Nanomaterials

#### 2.3.3.1 MB Adsorption from Single Contaminant Solutions

Methylene Blue (MB; Figure 4a) is a cationic dye and medical contrast agent, which has been widely used as a model contaminant for water treatment processes [8]. Because of its positive charge, MB is highly soluble in water with a hydrated form containing one molecule of water per molecule of MB [94]. The ionization of MB remains unchanged over a wide range of pH values [91]. Its conjugated  $\pi$ -electron system determines the UV/vis adsorption spectrum of MB in water (Figure 4c). The peaks in the UV-range result from the absorbance of the three aromatic rings, while the main peak at 664 nm is attributed to the absorbance of the whole conjugated  $\pi$ -electron system. The shoulder peak at 605 nm shows that MB also occurs as a dimer (Figure 4b) in solution, as  $\pi - \pi$  interactions between two MB molecules cause a shift to lower wavelengths in the absorption of the conjugated electron system [95]. The MB dimer is a hexahydrate in solution [94].

Besides interactions with molecules of the same species, MB is attracted to GO and rGO surfaces through both electrostatic interactions with the surface functional groups and  $\pi - \pi$  stacking [96, 97]. Sui et al [93] demonstrated the significance of electrostatic attraction for MB adsorption by

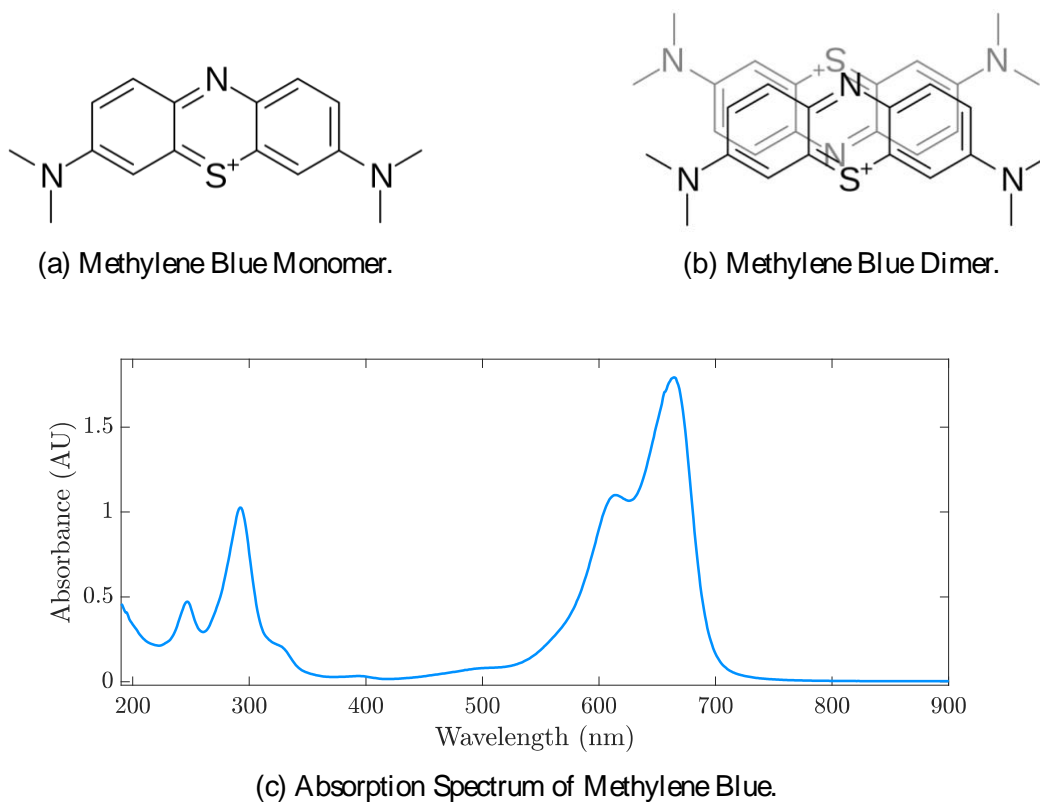


**Figure 4.** Methylene blue is a common model contaminant for wastewater treatment studies. Because of its bright blue color, it is commonly quantified in solution using UV/vis spectrometry.

preparing structurally similar but chemically different rGO-CNT hydrogels, reporting an increase in MB removal by almost 50 % as the atomic oxygen content of the adsorbent increases from 7.14 % to 10.24 %. Other authors have also related the adsorption capacity of 3DGSs for cationic dyes to their surface charge density [20, 53, 98]. Furthermore, as expected for electrostatic adsorption, MB removal increases proportionally to the initial pH value of the adsorbate solution [99]. At pH values below the point of zero charge, MB adsorbs to the rGO structure through  $\pi - \pi$  stacking, counteracting the electrostatic repulsion between the protonated surface and the cationic contaminant. As the solution pH increases, MB competes with protons for the adsorption sites until the competition becomes negligible at high pH values [89].

By demonstrating significant MB removal with a super-hydrophobic graphene structure, Wang et al [100] confirm that  $\pi - \pi$  interactions dominate the adsorption of the cationic dye at low surface charges. But also 3DGSs with heavily charged surfaces show a better removal of benzene-

containing cationic dyes than of non-aromatic cations [96], indicating that the synergistic effects of  $\pi - \pi$  and electrostatic interactions explain the exceptional adsorption of MB on 3DGSs [19].

The adsorption capacity of GO for MB also increases with the ionic strength [91]. Inorganic ions in solution are surrounded by water molecules. As the concentration of ions in solution increases, these ions start to interact with the hydrated organic ions, such as MB or the surface groups of GO. Because the interaction between the inorganic ions and water is more favorable than the interaction between the organic compounds and water, the physical bonds between water and the organic molecule become weaker. This lowers the energetic barrier for the adsorption, as the dehydration of the active sites of the adsorbate and the adsorbent makes up a large part of the activation energy of the adsorption. Furthermore, the solubility of the adsorbate decreases, which shifts the solution equilibrium of the organic compound towards the crystalline phase, such that MB might precipitate on the adsorbent. On the other hand, the removal of the positively charged MB could also be reduced through charge shielding by the dissolved ions [101].

Besides the chemical characteristics of the adsorbent and the background solution, the morphology of 3DGSs also influences the removal of MB. The adsorption capacity of graphene-based adsorbents increases in proportion to their specific surface area, when the surface chemistry of the adsorbent is kept constant [53, 66, 102, 103]. However, the theoretical surface area of porous carbon materials often exceeds their effective surface area, as pores are insufficiently interconnected, isolating pores in the core of 3DGSs [8]. Tao and co-workers [21] synthesized a 3DGS that exceeds the MB adsorption capacity of activated carbon with a similar surface area by more than 400 %, because its inner adsorption sites are available through a hierarchical spheroidal pore structure. The combination of micro- and mesopores with macropores allows for sufficient mass transport without significantly compromising the surface area of the material and therefore the number of adsorption sites [104].

Even when the effective surface area is comparable to the theoretical surface area of the adsorbent, mass transport is often the rate determining step in the removal of MB and other organic dyes [66], as dye removal is a successive process of dye diffusion through the boundary layer, intraparticle diffusion and adsorption onto the GBNM surface [20]. By comparing fits of kinetic adsorption measurements to the homogeneous surface diffusion model and to pseudo second order adsorption kinetics, Wang and Giammar [105] demonstrated that previously identified pseudo second order adsorption mechanisms might actually better fit mass transport controlled adsorption kinetics. If

the adsorbate solution is well-mixed, adsorbents with larger pore diameters show faster removal than those with smaller pores [67].

### 2.3.3.2 MB Adsorption from Complex Waters

Co-contaminants might also influence the adsorption capacity and adsorption rate of 3DGSs for specific pollutants through competitive adsorption, pore blocking or masking of surface functional groups. Natural organic matter (NOM), which consists of large aromatic molecules with an abundance of oxygen functional groups, has been shown to interact with GBNMs [106]. As expected by its molecular structures, the adsorption of NOM by oxidized GBNMs shows a strong pH dependence. At low pH values, the oxygen functional groups on both GO/rGO and NOM are protonated, such that NOM is bound to the adsorbent through both  $\pi - \pi$  stacking and hydrogen bonding. As the pH increases, the oxygen functional groups deprotonate and electrostatic repulsion between the then negatively charged species counteracts their  $\pi - \pi$  attraction, decreasing the adsorption capacity of GO/rGO for NOM. Furthermore, the large NOM molecules are more coiled at low pH values, because of hydrophobic interactions and the lack of electrostatic repulsion between the functional groups [107]. When the oxygen functional groups are negatively charged at high pH values, the structure stretches out as a result of electrostatic repulsion and takes up more space when bound to the adsorbent, decreasing its removal capacity. An increase in ionic strength of the solution has a similar effect as a decrease in pH. At higher ionic strength, the NOM molecules are in a more coiled configuration, so that the adsorption capacity for NOM is higher than at lower ionic strengths.

Depending on the morphology and the surface chemistry of the adsorbent, NOM might enhance or inhibit the removal of MB [108]. In the presence of NOM, heavy metal adsorption on GO is higher if the NOM adds charge to the surface [109] and is inhibited if NOM masks the surface charges [110]. As MB removal is also proportional to the surface charge density, a similar effect might govern the simultaneous removal of MB and NOM. However, the large NOM molecules also lower the specific surface area of the adsorbent or even block whole pores [83, 101], counteracting the potential increase in charge density. De Ridder et al. [101] attribute an observed decrease in adsorption capacity of MB on wastewater pre-loaded GAC to pore blocking by biopolymers. However, they also suspect that the decrease in MB adsorption could be related to a change in surface charge compared to pristine GAC. In general, smaller pores, as found in GAC [111], are more prone to pore blocking than larger and hierarchically distributed pores, which can

be formed in the synthesis of 3DGSs [83]. Despite its environmental relevance, the role of NOM co-contamination has not been systematically studied for the removal of organic pollutants by 3DGSs [8].

### 3 Graphene Oxide Sponge as Adsorbent for Organic Contaminants: Comparison with Granular Activated Carbon and Influence of Water Chemistry

**Abstract.** There is growing interest in graphene oxide (GO) as an adsorbent for recalcitrant organic contaminants, such as industrial dyes and pharmaceutical compounds, because of its high specific surface area, amphiphilic character and high mechanical strength. GO nanosheets can be self-assembled into three-dimensional porous sponges to facilitate their removal from treated waters. Although a number of chemically and structurally diverse sponges have been fabricated for the removal of anthropogenic water pollutants, adsorption studies have mostly been limited to single contaminant solutions, omitting the environmentally relevant effect of organic co-contaminants and inorganic ions on the adsorption process. Furthermore, the adsorptive performance of the novel material is rarely compared to the industrial standard, granular activated carbon. In this work, we show that a reduced graphene oxide (rGO)-cellulose nanocrystal sponge has a higher initial adsorption rate and specific adsorption capacity for the model dye methylene blue than a commonly used commercial granular activated carbon. While the adsorption of methylene blue on the sponge is not influenced by environmentally relevant concentrations of natural organic matter, organic co-contamination inhibits the removal of the dye by granular activated carbon. Ionic strength and pH of the contaminant solution do not significantly impact the performance of the sponge. Differences in adsorptive performance between the sponge and GAC are attributed to differences in the surface chemistry and pore structure of the adsorbents.

**Environmental Significance Statement.** With the development of nano-enabled technologies for environmental applications such as catalytic degradation and adsorption of water pollutants, questions about their sustainability and economic efficiency arise. In particular, nano-enabled technologies that are meant to replace existing non-nanotechnologies should be compared to the current industrial standard under environmentally relevant conditions to evaluate their benefit. Hence, this study aims at comparing the adsorptive performance of a graphene oxide sponge to granular activated carbon in a complex water and at understanding the influence of water chemistry on the adsorption of the model contaminant methylene blue on the sponge. The study identifies strengths and weaknesses of the nano-enabled adsorbent, such that further material development can preserve the benefits while addressing shortcomings.

### 3.1 Introduction

Three-dimensional assembly of nanosheets has recently been identified as a promising approach for the fabrication of sorbents for a wide range of contaminants [102, 112-115]. Combining the advantages of bulk solids and nanomaterials, these structures allow for easy separation from liquids and practical handling, while maintaining an exceptional specific surface area [23]. Among the most common of these materials are graphene-based hydrogels or sponges, which have also been used as targeted drug delivery systems [116] and supercapacitors [73]. However, these structures generally tend to be mechanically weak, which impairs their re-usability and might result in nanosheet release during use. Thus, the mechanical properties of graphene-based macrostructures have been enhanced through the incorporation of polymers [66, 67, 69], or one-dimensional nanomaterials such as cellulose nanocrystals (CNC) [12] and carbon nanotubes [89, 117, 118]. To create hierarchical pore systems that facilitate contaminant diffusion to sorption sites on the surface of the nanomaterial [12, 21, 55, 78], three-dimensional graphene-based structures have been formed around templates [12, 78] or gaseous spacers [53, 55]. The resulting pore size distribution determines the fraction of the sorbent surface that is accessible to the sorbate [83].

Furthermore, the synthesis method strongly influences the chemical composition of these sorbents [119]. Most graphene-based macrostructures contain a mixture of pristine, aromatic carbon

domains and areas functionalized with hydroxyl, epoxy, carbonyl and carboxyl groups [18]. Thus, they can interact with various sorbates through both polar and non-polar interactions [66]. Of special interest for the removal of organic contaminants are  $\pi - \pi$  interactions, which occur between systems of delocalized electrons. Additionally, hydrophobic interactions and polar removal mechanisms such as hydrogen and electrostatic bonding are mechanisms of contaminant adsorption from water [119]. The dominant interaction mechanism in the removal of a target pollutant by a graphene-based macrostructure is determined by the chemistries of both the adsorbent and the adsorbate, and the morphology and pore architecture of the adsorbent [8]. The ionic strength and pH of the background solution can also influence the dominant adsorption mechanisms [89].

The sorption capacity of graphene-based macrostructures for the common model dye methylene blue (MB) [66, 89, 96, 99] has been extensively studied; however, the effect of water chemistry on the removal of MB is often neglected. Furthermore, novel three-dimensional graphene-based structures are rarely compared to industrial standard sorbents [105, 120, 121]. Besides obtaining directly relatable sorption parameters, the juxtaposition of graphene-based sorbents and chemically similar, but structurally different materials deepens the understanding of the influence of mass transport on the sorption process. Granulated activated carbon (GAC), which consists of partially oxidized, interconnected layers of hexagonally arranged carbon atoms that are assembled into (micro)porous structures [122], is widely used in the removal of organic and inorganic contaminants from waters. The similar chemistries of GAC and three-dimensional graphene-based macrostructures and their significant differences in pore architecture make the comparison between these two sorbents especially interesting.

While laboratory scale sorption tests with single-compound solutions yield relevant theoretical sorption parameters, competitive sorption from complex waters containing natural organic matter (NOM) is a more realistic scenario. Apul et al [121] reported that interactions between NOM and graphene oxide (GO) nanosheets inhibit the adsorption of selected organic contaminants through direct adsorption competition. Because of the large surface area of the well dispersed GO sheets and electrostatic repulsion between the oxygen functional groups of GO and NOM, the competition for the adsorption sites is less significant than on pristine graphene, carbon nanotubes and GAC [121]. Besides direct competition, pore blocking reduces the adsorption capacity of porous solids for the target pollutant [101]. To determine the dominant mechanism in the competitive adsorption of MB from complex waters, Pelekani et al. [83] investigated the simultaneous removal of atrazine

and MB from deionized water by activated carbon fibers. They found that direct adsorption competition and pore blocking due to the presence of another contaminant strongly depend on the pore size and pore volume of the sorbent. Contrary to competitive adsorption, NOM adsorption on graphene-based adsorbents may also increase the adsorption capacity for cationic contaminants if the adsorbed NOM increases the oxygen functionality of the surface [106, 108, 123]. Furthermore, MB and NOM co-precipitate at high contaminant concentrations, such that the overall removal of MB from complex waters can be higher than from single-contaminant solutions [91].

As a result of fluctuations in wastewater generation over the course of a day and year, and environmental factors such as precipitation, the composition of municipal wastewaters varies strongly [124]. Industrial wastewaters can exhibit a wide range of pHs, ionic strengths and organic co-pollutants which can cause fouling of the adsorbent. Thus, it is crucial to not only determine the adsorption capacity of a target pollutant from single-contaminant solutions, but to also investigate the effect of water composition on the performance of the adsorbent. In buffered solutions, the adsorption capacity of MB on GO increases with pH [125, 126]. While the pH does not significantly affect the ionization of MB, more oxygen functional groups of GO deprotonate as the pH increases [91]. The higher surface charge causes stronger electrostatic attraction of MB to the adsorbent, but also the formation of water clusters around the ionic domains of the GO sheets [123] and MB [91], which hinder the attachment of MB to the surface. Hence, an increase in ionic strength facilitates the adsorption of MB on GO, as the ions reduce the interaction between water and the charged domains of adsorbate and adsorbent [91]. However, the effect of water chemistry (namely, ionic strength, pH and NOM content) on the removal of organic dyes by graphene-based macrostructures has not been systematically investigated. Furthermore, a comparison to the current industrial standard under these more realistic conditions is crucial when evaluating novel nanomaterial based adsorbents [105]. Hence, this study examines the adsorption of the model dye MB on a reduced graphene oxide (rGO)-cellulose nanocrystal (CNC) sponge under environmentally relevant conditions and compares the performance of the sponge to that of a common commercial GAC.

## 3.2 Materials and Methods

### 3.2.1 Preparation of rGO-CNC Sponges

The synthesis of the rGO-CNC sponges is described elsewhere [12], with slight modifications. Namely, the CNCs used in this study were sulfonated instead of carboxylated. In brief, a 4 mg/mL GO dispersion and a 40 mg/mL CNC dispersion were prepared from graphite (Ausbury Mills) and CNC powder (CelluForce), respectively. Then, 8.5 g of the GO dispersion, 0.5 mL of the CNC dispersion and 6 g of vitamin C (VC; Sigma-Aldrich) were vortexed in a cylindrical glass vial for 5 min. The vials were sonicated for 5 min before they were placed in a water bath at 90-95 °C for 2 min. After the initial pre-heating, the vials were sonicated for 1 min, re-heated for another 2 min and sonicated for 1 min again. Subsequently, the vials were placed in the water bath for 10 min, such that the GO nanosheets and CNCs self-assemble to form a porous sponge. To solidify the structure, approximately 30 mL of hot reverse osmosis (RO) water were added to the newly formed sponge and the vials are kept in the water bath for another 45 min. After a brief cooling period, the sponges were washed with RO water at least five times to remove the unreacted VC. Subsequently, the sponges were stored in RO water at room temperature for 6 days and the storage water was replaced every 24 h to ensure the release of all excess VC.

### 3.2.2 Characterization of the Adsorbents

#### 3.2.2.1 Scanning Electron Microscopy

The pore architectures of GAC and the rGO-CNC sponges were studied using scanning electron microscopy (SEM, Hitachi SU3500). The as-received GAC granules were directly imaged using SEM, while sponges were freeze-fractured at -80 °C. The fractured sponges were lyophilized (Labconco Freeze Dryer, Thermo Fisher) at -80 °C and 0.2 mbar pressure. The resulting aerogels were studied using SEM with no requirement for conductive coating, since the partial chemical reduction of GO with VC resulted in restoration of the electrical conductivity of the sponges.

### 3.2.2.2 X-Ray Photoelectron Spectroscopy

The surface chemistries of GAC and the rGO-CNC sponges were studied using X-ray Photoelectron Spectroscopy (XPS, K-alpha Thermo Fisher). The as-received GAC granules and lyophilized sponges were imaged under  $10^{-8}$  mbar vacuum with a monochromatic aluminum  $K_{\alpha}$  X-ray source. Survey and high-resolution spectra were recorded for both samples. The atomic compositions of the samples were determined from survey spectra using the equipment's Avantage user-interface software. High resolution  $C_{1s}$  spectra were deconvoluted to their constituent peaks using XPSPEAK4.1 software.

### 3.2.3 Adsorption Experiments

200 mL contaminant solutions were prepared in 600 mL glass beakers using 500 mg/L MB (Sigma-Aldrich), 200 mg/L NOM (Suwannee River RO isolate, IHSS) and 0.2 M sodium nitrate (Sigma-Aldrich) stock solutions. The pH of the contaminant solutions was adjusted by adding a negligible volume of 0.01 M nitric acid (Fisher) or 0.01 M sodium hydroxide (Sigma-Aldrich) solution. 20 mg of GAC (Norit 1240W GAC, Cabot Corp) or half a rGO-CNC sponge, which is equivalent to 20 mg GO, were placed in a pre-wetted paper teabag (David's Tea). Teabags were used to prevent crumbling of the rGO-CNC sponges or GAC during mechanical stirring of the solutions. Using a larger amount of adsorbent for these experiments was prohibitive because of the time intensive synthesis of the rGO-CNC sponges. The teabag was hung into the contaminant solution, and the covered beakers with the contaminant mixture were placed on a platform shaker (New Brunswick Instruments) operating at 100 rpm. 200  $\mu$ L aliquots were taken immediately before the immersion of the adsorbent into the contaminant solution and at each time point. The aliquots were kept in autosampler vials with silanized inserts to avoid interaction of MB with the walls of the vials. To account for the removal of MB by the teabag, control experiments with an empty teabag were performed for all MB concentrations, ionic strengths and pHs. For each configuration, the contaminant removal was calculated from the difference between the initial contaminant concentration in solution and the concentration at the respective time points. By subtracting the adsorption onto the teabag from the overall adsorption, we obtain the adsorption on the rGO-CNC sponge or GAC.

$$q(t) = \frac{\left(c_i^{TB+Ads} - c^{TB+Ads}(t)\right) \cdot V}{m_{Ads}} - \frac{\left(c_i^{TB} - c^{TB}(t)\right) \cdot V}{m_{Ads}} \quad (1)$$

Here,  $q(t)$  is the mass of adsorbed contaminant normalized by the mass of the adsorbent  $m_{Ads}$  at time  $t$ .  $c^{TB+Ads}(t)$  and  $c^{TB}(t)$  are the contaminant concentrations in solution of the test beaker and the control beaker at this time  $t$ , respectively. The corresponding initial contaminant concentrations in solution are denoted as  $c_i^{TB+Ads}$  and  $c_i^{TB}$  and  $V$  is the volume of the adsorbate solution. The reported values are the mean of triplicates  $\pm$  one standard deviation.

In competitive adsorption experiments with NOM, the initial precipitation of MB-NOM agglomerates was determined by measuring the MB concentration in solution after 1 h of equilibration. The difference between the amount of MB that was initially added and the MB that remained in solution after 1 h is the amount of MB that precipitated  $q_P$ .

$$q_P = (c_i^{MB} - c_{1h}^{MB}) \cdot V \quad (2)$$

$c_i^{MB}$  is the MB concentration that was calculated from the added amount of MB and  $c_{1h}^{MB}$  is the measured MB concentration in solution after 1 h.

To determine the maximum adsorption capacity, the experimental equilibrium data was fitted to the Langmuir and the Freundlich adsorption isotherm models using the Levenberg-Marquardt algorithm in MATLAB®. The equations for the two models are given by

$$\frac{1}{q_e} = \frac{1}{b q^{max} c_e} + \frac{1}{q^{max}} \quad (3)$$

and

$$q_e = K_F c_e^{1/n}, \quad (4)$$

respectively.  $q_e$  is the specific equilibrium sorbed concentration,  $c_e$  is the contaminant concentration in solution at equilibrium, the maximum specific adsorption capacity  $q^{max}$  and  $b$  are the fitting parameters for the Langmuir isotherm, and  $K_F$  and  $n$  are fitting parameters of the Freundlich model. The initial adsorption rate for MB on both adsorbents was estimated by a linear least squares fit through the data points within the first 3 min after initial contact between the adsorbent and the adsorbate solution.

### 3.2.4 Quantification of MB and NOM

To minimize NOM interference in the detection of MB from complex waters, the MB was separated from other organic contaminants in the water matrix by reversed-phase, ion-pair high performance liquid chromatography (HPLC, Agilent 1200) on a C18 column (Agilent-Eclipse XDB-C18, 5  $\mu\text{m}$ , 4.6 mm  $\times$  150 mm). The mobile phase consisted of 50% acetonitrile (mobile phase A, HPLC grade, Sigma-Aldrich) and 50% 10 mM sodium phosphate (Fisher) buffer (mobile phase B). The pH of the buffer was adjusted to 7 by adding a small amount of 5 M sodium hydroxide (Fisher) after 0.1 vol% of the ion pairing agent trifluoroacetic acid (TFA, Fisher) was added to mobile phase B. The injection volume was 20  $\mu\text{L}$ /sample. The elution time of MB was  $7.8 \pm 0.2$  min at a flow rate of 1 mL/min and a separation temperature of 35  $^{\circ}\text{C}$ . The column effluent was analyzed on-line in a UV-vis detector (Agilent 1200) by absorbance at 664 nm. ChemStation software was used to control the run parameters and to analyze the data. The lower and upper detection limits for MB were 3 mg/L and 200 mg/L, respectively.

NOM was detected by UV-vis absorbance spectrometry using a 1 cm optical path-length disposable polystyrene cuvette on a BioMate 3S spectrophotometer (Thermo Scientific). A 0.01 M sodium nitrate solution was used as a blank to measure the absorbance at 350 nm. The lower detection limit for NOM was 1.5 mg/L.

## 3.3 Results and Discussion

### 3.3.1 Material Characterization

#### 3.3.1.1 Microstructure of rGO-CNC sponges and GAC granules

The microstructures of the adsorbents were studied by SEM (Figure 5). In line with our recent works on hierarchically porous rGO sponges [12, 127], the rGO-CNC sponge of this work also had a hierarchically porous architecture. The use of excess amounts of VC resulted in formation of

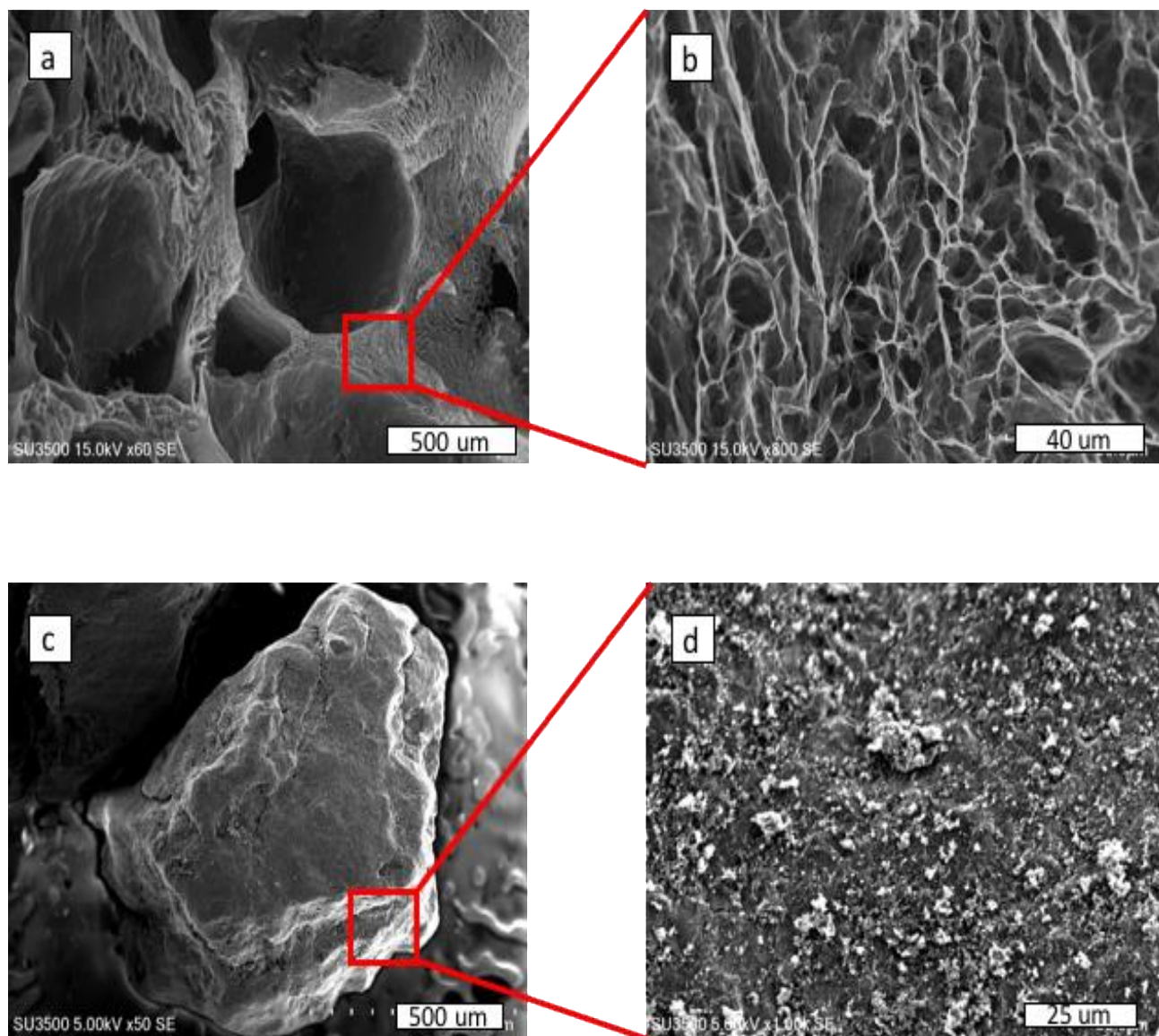


**Figure 5.** SEM micrographs of the (a) and (b) rGO-CNC sponges, and (c) and (d) GAC at (a) and (c) low, and (b) and (d) high magnifications. rGO-CNC sponges have a hierarchically porous architecture, whereas the surface of GAC is covered with small particulate matter.

millimeter-scale pores (Figure 5a), with pore walls that were also porous at the micron-scale (Figure 5b). The concentration of VC in the initial rGO-CNC colloidal dispersions (600 g/L) is well above its saturation concentration in water ( $\sim 330$  g/L). While the dissolved VC molecules chemically reduce GO, resulting in the formation of porous sponges with micron-sized pores, the excess amount of VC remains as solid undissolved grains that act as soft templates [12, 127]. The VC used in this work formed undissolved grains with diameters ranging from approximately a few

hundred microns to approximately one millimeter. Dissolution of these grains resulted in the formation of large pores of the same size range. We washed the sponges with copious amounts of water over the span of a few days to dissolve all the excess VC grains in the sponges. The resulting hierarchically porous sponges had an interconnected and open pore architecture at both millimeter and micrometer length scales [12].

The GAC granules had a strikingly different microstructure in comparison with rGO-CNC sponges (Figure 5c and d). The granule surfaces were relatively solid (Figure 5c), and upon magnification, the surfaces were covered with small debris-like particulate features. These small particles play a role in increasing the surface area of the GAC granules. Furthermore, micropores below 20 Å constitute most of the pore volume of bituminous steam activated GACs [128], such as the GAC used in this study. However, these below-nano-sized pores cannot be visualized through SEM imaging. While nitrogen adsorption is normally used for measuring the specific surface area of porous materials, we could not compare the specific surface area of rGO-CNC sponges and GAC side by side. The significant amount of oxygen containing functional groups of the sponges render them highly hydrophilic to the extent where complete removal of molecularly adsorbed water by freeze-drying becomes very challenging. The adsorbed water competes with nitrogen molecules that are usually used as probe gas for measuring the specific surface area of the porous materials, thus resulting in unreliable specific surface area measurements due to blockage of sponge active surface sites by water molecules.

### 3.3.1.2 Surface Chemistry of the Adsorbents

The surface chemistry of the adsorbents was studied using XPS. The atomic composition of the surfaces was determined by XPS survey scans (Figure 6a). Additionally, the high resolution C<sub>1s</sub> spectra of the samples were deconvoluted to their constituent peaks at 284.7 (sp<sup>2</sup> carbon), 285.5 (sp<sup>3</sup> carbon), 286.7 (hydroxyls), 287.6 (carbonyls and epoxides in case of the sponges [129, 130]), and 289 eV (carboxyls) (Figure 6b). A typical deconvolution of C<sub>1s</sub> peak is demonstrated in Figure 6c.

The surface of rGO-CNC sponges is more oxidized than the surface of the tested GAC based on the XPS survey scans (Figure 6a). The existence of more oxygen containing functional groups provides opportunities for interaction with a wide range of contaminants such as cationic dyes and dissolved organic matter. In addition, the rGO-CNC sponges contain a small amount of sulfur due

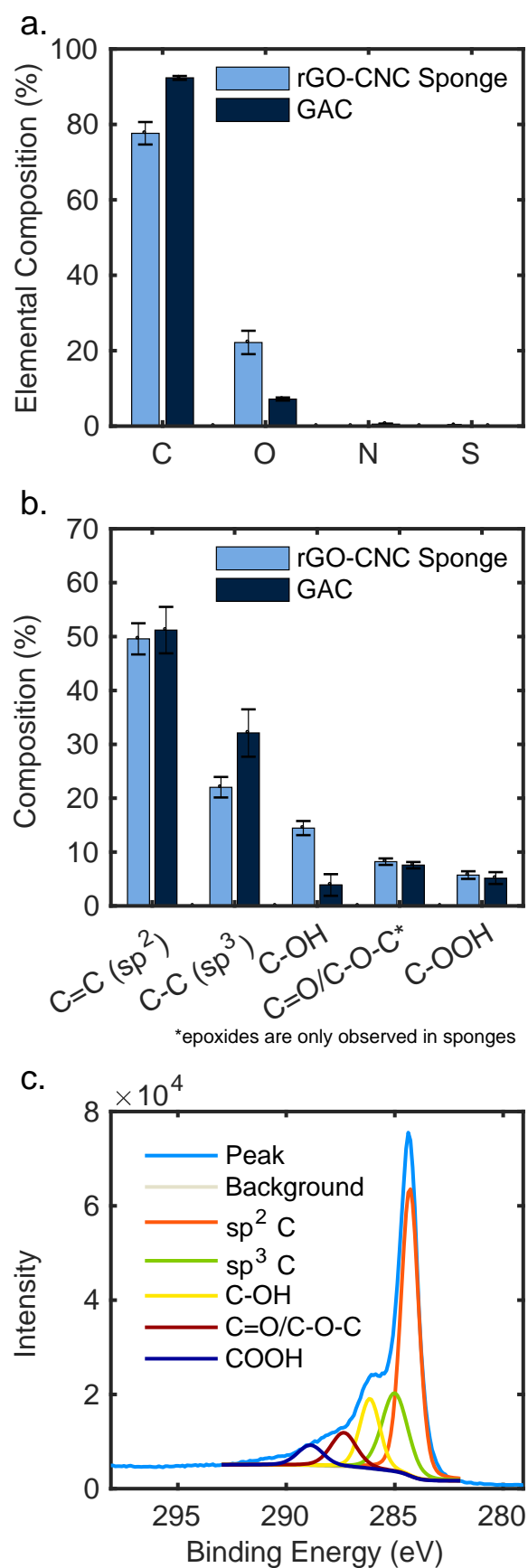


**Figure 6.** (a) Elemental analysis of the adsorbents. (b) Analysis of functional groups of the adsorbents. (c) Typical deconvolution of high resolution  $C_{1s}$  peak of a rGO-CNC sponge into its constituent sub-peaks, denoting  $sp^2$  carbon,  $sp^3$  carbon, hydroxyl, carbonyl/epoxide, and carboxyl groups.

to the sulfonated nature of CNCs that were used in this study. A trace amount of nitrogen was also detected in the GAC (Figure 6a).

Deconvolution of  $C_{1s}$  peaks of the rGO-CNC sponge and GAC also confirms that the sponges contain more oxygen containing functional groups than GAC (Figure 6b). While the amount of carbonyl and carboxyl groups of both sponges and GAC are relatively similar, the sponges are decorated with ~4 times more hydroxyl groups than GAC. The existence of more hydroxyl groups on sponges provide more opportunities for hydrogen bonding with target organic contaminants. Additionally, surface hydroxyls render sponges more hydrophilic than GAC. The higher amount of  $sp^3$  domains in GAC stems from the amorphous regions of the carbonaceous material.

### 3.3.2 Adsorption Studies

The experimental set-up for the adsorption experiments was designed to ensure that the pore structure of the adsorbent remains intact throughout the course of the experiment. This allows for a better analysis of mass transport phenomena in the adsorbent. However, even though the rGO-CNC sponge in this study is very strong compared to other reported three-dimensional graphene-based macrostructures for water treatment [12], a small amount of (r)GO was released from the rGO-CNC sponge during the adsorption experiment (Figure A1). The undesirable release could potentially be mitigated by further material engineering to strengthen the connection between the rGO sheets and CNCs. Improved homogenization of the self-assembly suspension minimizes the amount of unreduced GO in the sponge, such that hydrophobic interactions preserve the 3D structure upon immersion into water. Furthermore, an additional chemical strategy to crosslink the nanomaterials could improve the mechanical stability of the rGO-CNC sponge.

#### 3.3.2.1 Adsorption of MB on rGO-CNC Sponge and GAC

To determine the adsorption capacities of the rGO-CNC sponge and GAC for MB, the equilibrium removal of MB as a function of the equilibrium concentration of MB in solution is depicted in Figure 7a. As the time dependent removal after 16 h is statistically indistinguishable from the adsorption after 24 h (Figure A2), the equilibrium adsorption was approximated as the removal of MB after 24 h of exposure to the adsorbent. The specific adsorption capacity of the rGO-CNC sponge (~600 mg MB/g GO) is approximately three times higher than that of GAC (~200 mg MB/g

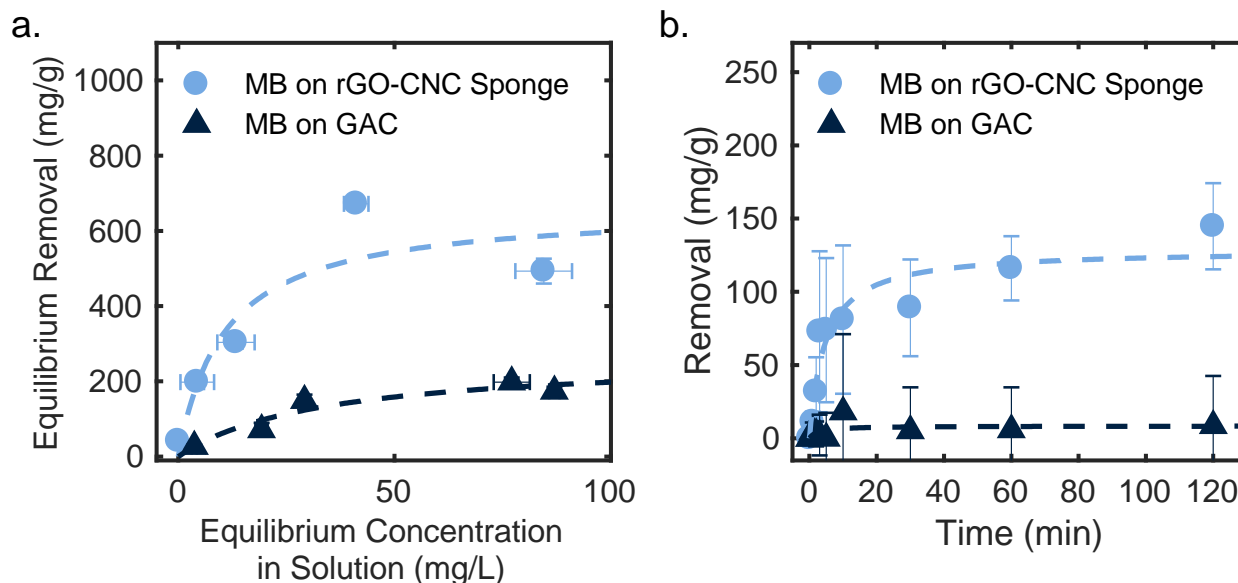


**Figure 7.** (a) Adsorption isotherms and (b) kinetics of MB adsorption on the rGO-CNC sponge and on GAC at an ionic strength of 0.01 M and pH 6. The kinetic experiment was performed at an initial MB concentration of 50 mg/L. The error bars represent one standard deviation.

GAC). As the adsorption capacity of an adsorbent increases with the number of adsorbate-specific adsorption sites, the higher MB removal of the rGO-CNC sponge can be attributed to both its larger accessible specific surface area and the differences in surface chemistry between the adsorbents. The removal of the positively charged organic structure of the MB molecule (Figure A3a) is proportional to the atomic oxygen content of carbonaceous adsorbents [93], which is directly related to their surface charge [20, 53]. Hence, the rGO-CNC sponge with its abundance of oxygen functional groups exhibits more MB-specific adsorption sites than GAC. Although we did not measure the surface area of the GO sponge, estimates from our earlier work with a GO-CNC sponge [12] suggest that the specific surface area is greater ( $\sim 2000 \text{ cm}^2/\text{g}$ ) than that of the GAC used here ( $1100 \text{ cm}^2/\text{g}$ ). Thus the rGO-CNC sponge can also spatially accommodate more MB molecules than GAC because of its larger effective surface area [66, 102].

The experimental data was fitted to the Langmuir and the Freundlich adsorption isotherms (Table 1). Adsorption on both the rGO-CNC sponge and GAC are best represented by the Langmuir model. Mechanistically, this behavior can be attributed to attractive interactions between the adsorbate and the adsorbent, and repulsive interactions between two MB molecules. The partially negatively charged oxygen functional groups on the surface of the rGO-CNC sponge and

GAC attract the positively charged MB molecules through electrostatic interactions [97]. The presence of abundant  $sp^2$  carbons also leads to  $\pi$ - $\pi$  interactions. Once the adsorbent surface is covered with MB, the surface charge becomes less negative, such that the adsorption of a second layer of MB molecules becomes energetically less favorable. Hence, the electrostatic repulsion between two MB molecules leads to monolayer instead of bulk adsorption of MB on the rGO-CNC sponge and GAC, even though the potential for  $\pi$ - $\pi$  interactions between MB and pristine adsorbent and surfaces previously covered with MB is similar. As one of the key assumptions of the Langmuir model is monolayer adsorption [79], the good isotherm fit supports the importance of surface area rather than pore volume for the adsorption of MB on the rGO-CNC sponge and GAC.

**Table 1.** Langmuir and Freundlich adsorption isotherm fitting parameters.

Adsorbent	Langmuir			Freundlich		
	$b$ [L/mg]	$q_{\max}$ [mg/g]	$R_2$	$n$ [-]	$K_F$ [mg $^{1-n}$ L $^n$ /g]	$R_2$
rGO-CNC sponge	0.094	660.3	0.852	3.4	160.9	0.784
Norit GAC	0.030	263.8	0.914	2.0	21.3	0.877

Besides the equilibrium removal behavior, the initial adsorption kinetics of MB is another interesting property of the adsorbent. Figure 7b shows the influence of contact time on MB removal by the rGO-CNC sponge and GAC. After 2 h, 10 times more MB is bound to the rGO-CNC sponge than to GAC. The initial adsorption rate of MB on the rGO-CNC sponge is 17.0 mg/(g s) ( $R_2 = 0.865$ ), which is approximately an order of magnitude higher than the initial adsorption rate on GAC. The bimodally distributed, larger pores of the rGO-CNC sponge facilitate intra-particle diffusion compared to the smaller more homogeneous pores of GAC. Hence, this suggests that the initial adsorption rate is mass transport controlled.

### 3.3.2.2 Influence of Ionic Strength and pH on MB Adsorption by the rGO-CNC sponge

To evaluate the performance of the rGO-CNC sponge in changing water chemistries, the pH and ionic strength of the contaminant solution were varied. Figure 8a shows the influence of ionic strength on the equilibrium removal of MB. The adsorption of MB increases by 38 % with an increase of  $NaNO_3$  concentration over two orders of magnitude. Yang et al [91] and Benaissa [131] observed the same trend for the adsorption of MB on GO sheets and GAC, respectively. As the

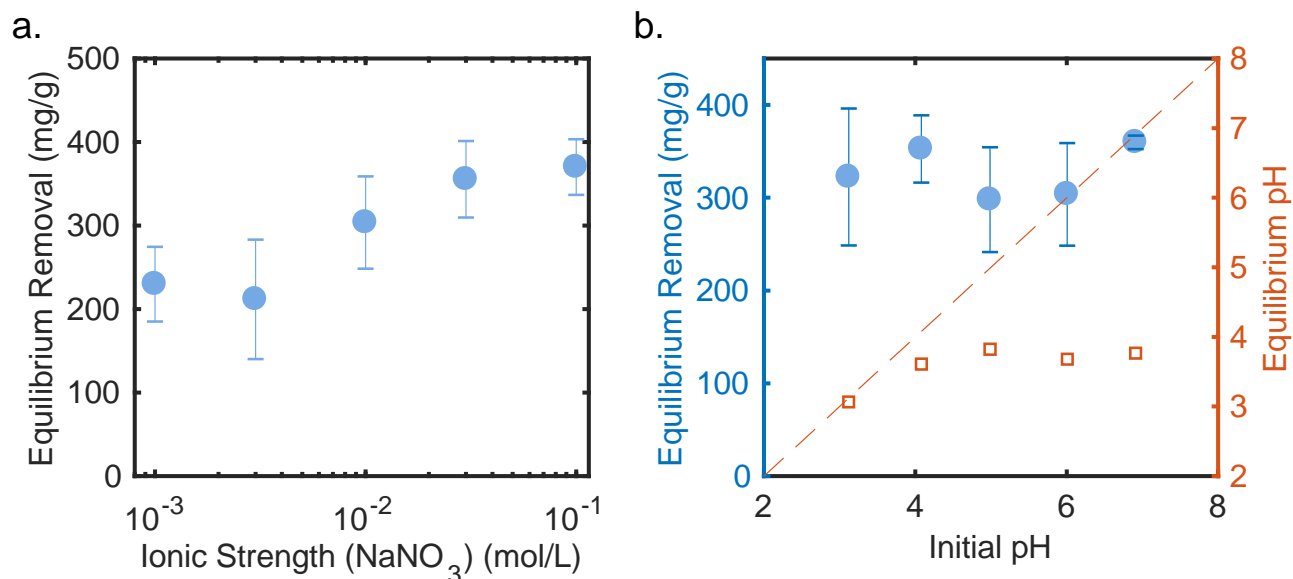


**Figure 8.** Effect of (a) ionic strength and (b) pH on the equilibrium adsorption of 50 mg/L MB by the rGO-CNC sponge. The pH was adjusted to 6 (a) and the ionic strength to 0.01 M NaNO<sub>3</sub> (b), respectively. The error bars represent one standard deviation.

contaminant molecules and the oxygen functional groups are less hydrated in the presence of inorganic ions [91], the energetic barrier for the adsorption of MB to GO is lower. In contrast, MB adsorption is stable over a wide range of environmentally relevant pH values (Figure 8b). The rGO-CNC sponge buffers the pH of the contaminant solution to  $3.7 \pm 0.1$  when the initial pH is above this threshold value specific to this rGO-CNC sponge [89]. The threshold value of carbonaceous adsorbents depends on the type and quantity of the oxygen functional groups [132, 133]. In this study, when the initial pH is below 3.7, it remains constant throughout the experiment. However, the protonation of the oxygen functional groups does not significantly change between pH 3 and pH 3.7 [134], such that the adsorption of MB remains approximately constant at these moderately acidic pH values. Hence, equilibrium MB adsorption on the rGO-CNC sponge is independent of the initial pH, if it is between pH 3 and pH 7.

### 3.3.2.3 MB Adsorption in the Presence of NOM

**Detection of MB in complex waters.** As MB and NOM interact with each other in solution (Figure A4), the MB concentration cannot be directly detected by UV-vis measurement in the presence of NOM. Instead, MB has to be separated from the NOM before quantification by absorbance.

Reversed phase HPLC separates compounds by their partition coefficient between the non-polar stationary phase and the polar mobile phase. Because both NOM and MB are charged organic phase and the polar mobile phase. Because both NOM and MB are charged organic molecules, their partition coefficients between the hydrophobic and hydrophilic phase and hence their elution times from the column are similar (Figure 9e). By introducing the ion pairing agent TFA (Figure A3b) to the system, MB can be retained in the column longer. The negatively charged polar end of the ion pairing agent selectively binds to the positively charged MB and the non-polar end interacts strongly with the stationary phase, which increases the affinity of the MB-TFA complex for the stationary phase. As the ion pairing agent is not attracted to the mostly negatively charged NOM, the elution time of the NOM is indifferent to the presence of TFA. Figures 9a and b show typical chromatograms of MB-NOM separation in the presence of TFA at 664 nm and 300 nm, which are the detection wavelengths for MB and NOM, respectively. The compounds are clearly separated, such that the spectra of the peaks (Figure 9c and d) correspond to the adsorption spectra of the NOM and MB, respectively.

**Competitive Adsorption of MB and NOM.** Naturally occurring organic contaminants contain both oxygen functional groups and aromatic rings, through which they can interact with carbonaceous adsorbents and MB. Fouling of the adsorbent surface by adsorption of organic co-contaminants may reduce the adsorption capacity of the adsorbent for the target pollutant. Figure 10a shows the adsorption of NOM on the rGO-CNC sponge and GAC as a function of NOM concentration in solution after 24 h of exposure. The kinetics of NOM removal are slower than the rate of MB adsorption. Thus, equilibrium is not quite reached after a contact time of 24 h between the NOM solution and the adsorbent, but the kinetic adsorption curve has relatively flattened out (Figure A5). After 24 h, the rGO-CNC sponge removes more than 200 mg NOM/g GO, which is approximately 40 times more than GAC. As the rGO-CNC sponge contains more oxygen functional groups and exhibits a larger surface area than GAC, there are more NOM adsorption sites for hydrogen bonding on the rGO-CNC sponge than on the industrial standard [110]. However, the ratio of the adsorption capacities of the two adsorbents (GAC:rGO-CNC sponge) is lower for the adsorption of NOM (1:40) than for MB removal (1:3). As the pores of GAC are smaller and more narrowly distributed in size, pore blocking by the large NOM molecules might significantly decrease the effective surface area of GAC [83]. In contrast, the larger bimodally distributed pores of the rGO-CNC sponge are too large to be blocked by NOM. Because MB is small enough to diffuse into the

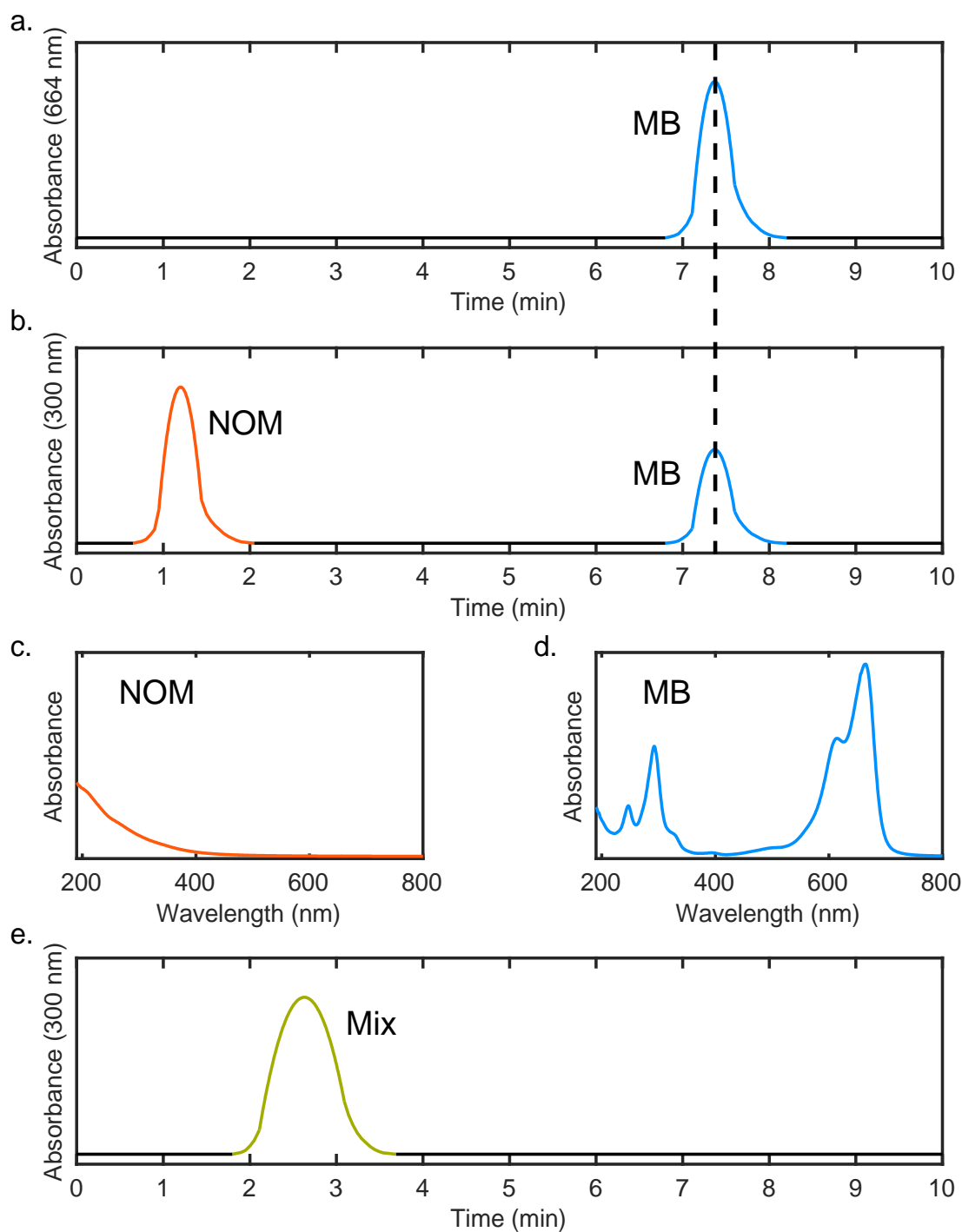


**Figure 9.** Typical chromatograms from the separation of MB and NOM at absorbances of (a) 664 nm and (b) 300 nm. The spectrum of the first elution peak corresponds to (c) the absorption spectrum of NOM and the second elution peak originates from (d) the characteristic absorption spectrum of MB. (e) Chromatogram of the MB-NOM mixture without TFA.

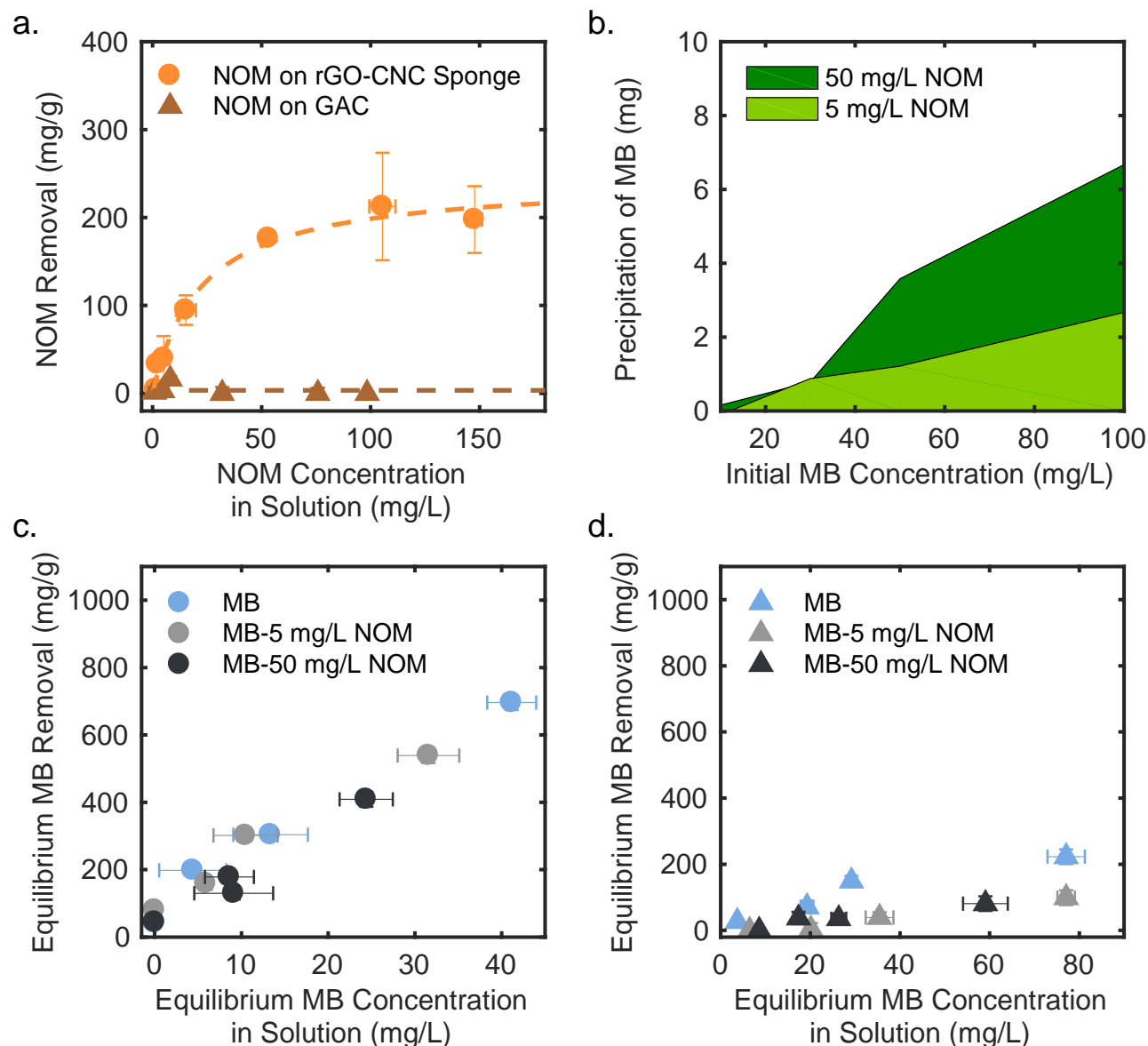


**Figure 10.** (a) Adsorption of NOM by the rGO-CNC sponge and GAC at an ionic strength of 0.01 M and pH 6. (b) In the presence of NOM, MB and NOM co-precipitate. (c) The removal of MB on the rGO-CNC sponge is not altered in the presence of high and low concentrations of NOM, (d) while the NOM that remains in solution after precipitation inhibits the adsorption of MB on GAC.

inner pores of GAC, it does not block its pores. As a result, the effective surface area of GAC for NOM adsorption is lower than for the removal of MB, while the effective surface area of the rGO-CNC sponge is similar for both adsorbates. Additionally, the rGO-CNC sponge might exhibit more NOM-specific adsorption sites than GAC.

To investigate the effect of NOM on the adsorption of MB by the two adsorbents, solutions containing MB and NOM were first equilibrated for 1 h. At the higher NOM concentration of 50 mg/L, there was visible precipitation of MB-NOM agglomerates after this equilibration period, but MB and NOM were also removed by precipitation in NOM solutions as low as 5 mg/L (Figure 10b). The amount of MB that remains dissolved depends on both the initial MB and the initial NOM concentrations. Because of the co-precipitation of MB and NOM, the initial effective MB concentration of these adsorption experiments, i.e. the MB concentration immediately before immersion of the adsorbent into the complex contaminant solution, is lower than in single-component adsorption studies. Thus, the direct comparison of MB removal from solutions to which the same amount of MB, but a different amount of NOM was added is not possible. A decrease in MB adsorption in the presence of NOM could result from a lower driving force because of a lower effective MB concentration and/or inhibition through competitive adsorption with NOM. To understand whether NOM hinders the adsorption of MB, Figures 10c and d show the adsorption of MB from complex waters of high and low NOM concentration as isotherms, comparing the adsorption behavior as a function of equilibrium MB concentration, rather than amount of MB that was added to the solution (i.e., these data take into account the mass of MB removed from solution by precipitation with NOM). This eliminates the influence of NOM-MB co-precipitation on adsorption, which allows for conclusions regarding competitive adsorption of MB and NOM.

Although the experimental measurements resemble the isotherm models in shape, the Langmuir and the Freundlich model are not appropriate to represent adsorption from multi-contaminant systems. Nonetheless, isotherms are still a useful qualitative indicator for the adsorption capacity of the respective systems. The equilibrium adsorption of MB in the presence of 5 mg/L and 50 mg/L NOM on the rGO-CNC sponge (Figure 10c) follows the same trend as the adsorption from pure MB solution. On the other hand, the removal of MB on GAC is equally inhibited at high and low NOM concentrations (Figure 10d). Similar to the self-inhibition of NOM, the smaller pores of the GAC are blocked off by NOM, such that the removal of MB is lower than from pure MB solutions [135]. 5 mg/L of NOM suffice to decrease the accessible surface area of GAC and there is no further inhibition with a 10-fold increase in NOM concentration.

Although NOM adsorbs to the rGO-CNC sponge, it did not affect the removal of MB on the rGO-CNC sponge in the range of MB and NOM concentrations we investigated. As the sponge is less prone to pore blocking than GAC, MB could be in direct competition with NOM for the adsorption

sites on the sponge. However, even at fairly high MB and NOM concentrations, the MB adsorption still follows the same isotherm as pure MB removal. Hence, it is more likely that MB interacts with NOM through  $\pi$ - $\pi$  stacking and electrostatic interactions to form another layer on previously adsorbed NOM and vice versa.

### 3.4 Conclusions

We have demonstrated that the rGO-CNC sponge outperforms the industrial standard GAC in the removal of MB from pure MB solutions and complex waters. MB adsorption on GAC is inhibited by NOM, which we attribute to a strong reduction of effective surface area through pore blocking. In contrast, the effective surface area of the sponge is not significantly compromised by NOM and adsorption might occur in multiple layers of NOM and MB. However, this study only tested one representative GAC. Future studies should evaluate different types of GAC and even more complex water chemistries. Because of its buffering capacity, MB sorption on the rGO-CNC sponge is stable from pH 3 to 7. The slight increase in adsorption capacity at higher ionic strengths likely results from the lower hydration of charged domains under these conditions.

## 4 Conclusions and Future Work

The rGO-CNC sponge outperforms the the tested GAC in the adsorption of the model contaminant MB. By comparing the removal of MB from complex waters, we showed that the rGO-CNC sponge could extend the classic applications of GAC. Because of the large specific surface area and the unique pore structure of the rGO-CNC sponge, which can only be achieved through the guided self-assembly of GO nanosheets, the adsorbent is less prone to pore blocking. Hence, the rGO-CNC sponge can remove larger molecules, such as NOM, more quickly and in a higher quantity than GAC. Furthermore, the adsorption of a target pollutant on the rGO-CNC sponge is less inhibited by small particles and large organic co-contaminants. To better understand adsorption mechanisms on the rGO-CNC sponge, more contaminants need to be explored and compared to find patterns in the adsorption capacity and rate.

By varying the ionic strength and pH of the adsorbate solution, we found that adsorption of MB on the rGO-CNC sponge is relatively stable over a wide range of environmentally relevant water chemistries. However, these experiments are performed under controlled conditions, with only one electrolyte and a limited number of possible interactions between electrolytes, organic contaminants and the adsorbent. Adsorption experiments with spiked surface waters or pre-treated wastewaters could act as stress tests for the rGO-CNC sponge to define the boundaries of the adsorbent.

The nanomaterial release and recyclability of graphene-based adsorbents for environmental applications also require further investigation. In general, the self-assembly of the nanosheets into 3DGSs facilitates the recovery of the adsorbent. Nevertheless, in the batch adsorption experiment, the rGO-CNC sponge releases a few nanoparticles even under fairly low mechanical stress. This brings up questions about the toxicity of GBNMs and their fate and transport in the environment. With this knowledge, scientists and agencies can establish release limits of GBNMs. Once critical concentrations have been stated, material scientists can work within these boundaries to incorporate

GBNMs into novel adsorbents and make use of their exceptional properties, without risking negative impacts on the environment.

Although the synthesis of rGO through oxidation and reduction is more sustainable than other methods, its environmental footprint is still significant due to the extensive use of harsh chemicals. Besides these environmental concerns, the large-scale production of GBNMs is more expensive than that of GAC. Hence, an efficient desorption and re-use technique must be established for 3DGSs to make them worth their economic and environmental investment. An alternative to using GBNMs as a bulk material would be to coat porous structures of a cheaper material with GBNMs, minimizing the material cost while maintaining its excellent surface properties.

While a lot of research remains to be done, graphene, GO and rGO are promising candidates for water treatment applications. Their versatile chemistry and large specific surface area together with their high mechanical strength is unmatched. The combination of these characteristics in one material offers myriad possibilities to harvest the benefits of GBNMs for environmental applications.

## Bibliography

1. Stankovich, S., et al., *Stable aqueous dispersions of graphitic nanoplatelets via the reduction of exfoliated graphite oxide in the presence of poly (sodium 4-styrenesulfonate)*. Journal of Materials Chemistry A, 2006. **16**(2): p. 155-158.
2. Zhang, J., et al., *Reduction of graphene oxide via L-ascorbic acid*. Chemical Communications, 2010. **46**(7): p. 1112-1114.
3. Park, S. and R.S. Ruoff, *Chemical methods for the production of graphenes*. Nature Nanotechnology, 2009. **4**(4): p. 217.
4. Kim, T.-H., et al., *Full-colour quantum dot displays fabricated by transfer printing*. Nature Photonics, 2011. **5**(3): p. 176.
5. Bourzac, K., *Quantum dots go on display*. Nature News, 2013. **493**(7432): p. 283.
6. Jaroenworarluck, A., et al., *Characteristics of silica-coated TiO<sub>2</sub> and its UV absorption for sunscreen cosmetic applications*. Surface and Interface Analysis: An International Journal devoted to the development and application of techniques for the analysis of surfaces, interfaces and thin films, 2006. **38**(4): p. 473-477.
7. Liu, Y.-L. and J.M. Wu, *Synergistically catalytic activities of BiFeO<sub>3</sub>/TiO<sub>2</sub> core-shell nanocomposites for degradation of organic dye molecule through piezophototronic effect*. Nano Energy, 2019. **56**: p. 74-81.
8. Yousefi, N., et al., *Environmental performance of graphene-based 3D macrostructures*. Nature Nanotechnology, 2019: p. 1.
9. Masikini, M., et al., *Electrochemical Sensor Based on Multi-walled Carbon Nanotube/Gold Nanoparticle Modified Glassy Carbon Electrode for Detection of Estradiol in Environmental Samples*. Electroanalysis, 2019.

10. Balapanuru, J., et al., *Desalination properties of a free-standing, partially oxidized few-layer graphene membrane*. *Desalination*, 2019. **451**: p. 72-80.
11. Al-Attabi, R., et al., *One-pot synthesis of catalytic molybdenum based nanocomposite nano-fiber membranes for aerosol air remediation*. *Science of the Total Environment*, 2019. **647**: p. 725-733.
12. Yousefi, N., et al., *Hierarchically porous, ultra-strong reduced graphene oxide-cellulose nanocrystal sponges for exceptional adsorption of water contaminants*. *Nanoscale*, 2018. **10**(15): p. 7171-7184.
13. Jastrzębska, A.M. and A.R. Olszyna, *The ecotoxicity of graphene family materials: current status, knowledge gaps and future needs*. *Journal of Nanoparticle Research*, 2015. **17**(1): p. 40.
14. Lanphere, J.D., C.J. Luth, and S.L. Walker, *Effects of solution chemistry on the transport of graphene oxide in saturated porous media*. *Environmental Science & Technology*, 2013. **47**(9): p. 4255-4261.
15. Zhao, J., et al., *Graphene in the aquatic environment: adsorption, dispersion, toxicity and transformation*. *Environmental Science & Technology*, 2014. **48**(17): p. 9995-10009.
16. Chabot, V., et al., *A review of graphene and graphene oxide sponge: material synthesis and applications to energy and the environment*. *Energy & Environmental Science*, 2014. **7**(5): p. 1564-1596.
17. He, H., et al., *A new structural model for graphite oxide*. *Chemical Physics Letters*, 1998. **287**(1-2): p. 53-56.
18. Lerf, A., et al., *Structure of graphite oxide revisited*. *The Journal of Physical Chemistry B*, 1998. **102**(23): p. 4477-4482.
19. Shen, Y., Q. Fang, and B. Chen, *Environmental applications of three-dimensional graphene-based macrostructures: adsorption, transformation, and detection*. *Environmental Science & Technology*, 2014. **49**(1): p. 67-84.
20. Deng, J., et al., *Toward 3D graphene oxide gels based adsorbents for high-efficient water treatment via the promotion of biopolymers*. *Journal of Hazardous Materials*, 2013. **263**: p. 467-478.
21. Tao, Y., et al., *Monolithic carbons with spheroidal and hierarchical pores produced by the linkage of functionalized graphene sheets*. *Carbon*, 2014. **69**: p. 169-177.

22. Loh, K.P., et al., *The chemistry of graphene*. Journal of Materials Chemistry A, 2010. **20**(12): p. 2277-2289.
23. Stoller, M.D., et al., *Graphene-based ultracapacitors*. Nano Letters, 2008. **8**(10): p. 3498-3502.
24. Novoselov, K.S., et al., *Electric field effect in atomically thin carbon films*. Science, 2004. **306**(5696): p. 666-669.
25. Balandin, A.A., *Thermal properties of graphene, carbon nanotubes and nanostructured carbon materials*. Nature Materials, 2011. **10**(8): p. 569.
26. Lee, C., et al., *Measurement of the elastic properties and intrinsic strength of monolayer graphene*. Science, 2008. **321**(5887): p. 385-388.
27. Ohta, T., et al., *Controlling the electronic structure of bilayer graphene*. Science, 2006. **313**(5789): p. 951-954.
28. Kim, K.S., et al., *Large-scale pattern growth of graphene films for stretchable transparent electrodes*. Nature, 2009. **457**(7230): p. 706.
29. Bae, S., et al., *Roll-to-roll production of 30-inch graphene films for transparent electrodes*. Nature Nanotechnology, 2010. **5**(8): p. 574.
30. Reina, A., et al., *Growth of large-area single-and bi-layer graphene by controlled carbon precipitation on polycrystalline Ni surfaces*. Nano Research, 2009. **2**(6): p. 509-516.
31. Yu, Q., et al., *Graphene segregated on Ni surfaces and transferred to insulators*. Applied Physics Letters, 2008. **93**(11): p. 113103.
32. Choi, W., et al., *Synthesis of graphene and its applications: a review*. Critical Reviews in Solid State and Materials Sciences, 2010. **35**(1): p. 52-71.
33. Lotya, M., et al., *Liquid phase production of graphene by exfoliation of graphite in surfactant/water solutions*. Journal of the American Chemical Society, 2009. **131**(10): p. 3611-3620.
34. Hernandez, Y., et al., *High-yield production of graphene by liquid-phase exfoliation of graphite*. Nature Nanotechnology, 2008. **3**(9): p. 563.
35. Novoselov, K.S., et al., *A roadmap for graphene*. Nature, 2012. **490**: p. 192.

36. He, H., et al., *A new structural model for graphite oxide*. Chemical Physics Letters, 1998. **287**(1): p. 53-56.
37. Hummers Jr, W.S. and R.E. Offeman, *Preparation of graphitic oxide*. Journal of the American Chemical Society, 1958. **80**(6): p. 1339-1339.
38. Marcano, D.C., et al., *Improved synthesis of graphene oxide*. ACS nano, 2010. **4**(8): p. 4806-4814.
39. Chen, J., et al., *An improved Hummers method for eco-friendly synthesis of graphene oxide*. Carbon, 2013. **64**: p. 225-229.
40. Brodie, B., *Sur le poids atomique du graphite*. Ann. Chim. Phys, 1860. **59**(466): p. e472.
41. Staudenmaier, L., *Verfahren zur darstellung der graphitsäure*. European Journal of Inorganic Chemistry, 1898. **31**(2): p. 1481-1487.
42. Zhang, X., et al., *Mechanically strong and highly conductive graphene aerogel and its use as electrodes for electrochemical power sources*. Journal of Materials Chemistry, 2011. **21**(18): p. 6494-6497.
43. Zhang, H.-B., et al., *Vacuum-assisted synthesis of graphene from thermal exfoliation and reduction of graphite oxide*. Journal of Materials Chemistry A, 2011. **21**(14): p. 5392-5397.
44. Stankovich, S., et al., *Synthesis of graphene-based nanosheets via chemical reduction of exfoliated graphite oxide*. Carbon, 2007. **45**(7): p. 1558-1565.
45. Fernández, M., et al., *Vitamin C is an ideal substitute for hydrazine in the reduction of graphene oxide suspensions*. Journal of Physical Chemistry C, 2010. **114**: p. 6426-6432.
46. Shin, H.J., et al., *Efficient reduction of graphite oxide by sodium borohydride and its effect on electrical conductance*. Advanced Functional Materials, 2009. **19**(12): p. 1987-1992.
47. Tang, C.-Y., et al., *Tannic acid functionalized graphene hydrogel for organic dye adsorption*. Ecotoxicology and Environmental Safety, 2018. **165**: p. 299-306.
48. Wang, J., et al., *Self-assembly of graphene into three-dimensional structures promoted by natural phenolic acids*. Journal of Materials Chemistry A, 2012. **22**(42): p. 22459-22466.
49. Gao, Y. and Z. Tang, *Design and application of inorganic nanoparticle superstructures: current status and future challenges*. Small, 2011. **7**(15): p. 2133-2146.

50. Appel, E.A., et al., *Ultrahigh-water-content supramolecular hydrogels exhibiting multistimuli responsiveness*. Journal of the American Chemical Society, 2012. **134**(28): p. 11767-11773.
51. IUPAC, *Compendium of Chemical Terminology*. 2 ed., Oxford: Blackwell Scientific Publications.
52. Pierre, A.C. and G.M. Pajonk, *Chemistry of aerogels and their applications*. Chemical Reviews, 2002. **102**(11): p. 4243-4266.
53. Zhao, J., W. Ren, and H.-M. Cheng, *Graphene sponge for efficient and repeatable adsorption and desorption of water contaminations*. Journal of Materials Chemistry, 2012. **22**(38): p. 20197-20202.
54. Zhao, Y., et al., *A versatile, ultralight, nitrogen-doped graphene framework*. Angewandte Chemie, 2012. **124**(45): p. 11533-11537.
55. Niu, Z., et al., *A leavening strategy to prepare reduced graphene oxide foams*. Advanced Materials, 2012. **24**(30): p. 4144-4150.
56. Chen, Z., et al., *Three-dimensional flexible and conductive interconnected graphene networks grown by chemical vapour deposition*. Nature Materials, 2011. **10**(6): p. 424-428.
57. Dong, X., et al., *Superhydrophobic and superoleophilic hybrid foam of graphene and carbon nanotube for selective removal of oils or organic solvents from the surface of water*. Chemical Communications, 2012. **48**(86): p. 10660-10662.
58. Bong, J., et al., *Dynamic graphene filters for selective gas-water-oil separation*. Scientific Reports, 2015. **5**: p. 14321.
59. Derjaguin, B.v. and L. Landau, *Theory of the stability of strongly charged lyophobic sols and of the adhesion of strongly charged particles in solutions of electrolytes*. Progress in Surface Science, 1993. **43**(1-4): p. 30-59.
60. Verwey, E.J.W., J.T.G. Overbeek, and K. Van Nes, *Theory of the stability of lyophobic colloids: the interaction of sol particles having an electric double layer*. 1948: Elsevier Publishing Company.
61. Huang, H., et al., *Glucono- $\delta$ -lactone controlled assembly of graphene oxide hydrogels with selectively reversible gel-sol transition*. Soft Matter, 2012. **8**(17): p. 4609-4615.
62. Bai, H., et al., *On the gelation of graphene oxide*. The Journal of Physical Chemistry C, 2011. **115**(13): p. 5545-5551.

63. Xu, Y., et al., *Self-assembled graphene hydrogel via a one-step hydrothermal process*. ACS Nano, 2010. **4**(7): p. 4324-4330.
64. Zhao, Y., et al., *Highly compression-tolerant supercapacitor based on polypyrrole-mediated graphene foam electrodes*. Advanced materials, 2013. **25**(4): p. 591-595.
65. Qiu, L., et al., *Biomimetic superelastic graphene-based cellular monoliths*. Nature communications, 2012. **3**: p. 1241.
66. Chen, Y., et al., *Graphene oxide–chitosan composite hydrogels as broad-spectrum adsorbents for water purification*. Journal of Materials Chemistry A, 2013. **1**(6): p. 1992-2001.
67. Sui, Z.-Y., et al., *Preparation of three-dimensional graphene oxide–polyethylenimine porous materials as dye and gas adsorbents*. ACS Applied Materials & Interfaces, 2013. **5**(18): p. 9172-9179.
68. Shen, J., et al., *Study on graphene-oxide-based polyacrylamide composite hydrogels*. Composites Part A: Applied Science Manufacturing, 2012. **43**(9): p. 1476-1481.
69. Xu, Y., et al., *Three-dimensional self-assembly of graphene oxide and DNA into multifunctional hydrogels*. ACS Nano, 2010. **4**(12): p. 7358-7362.
70. Adhikari, B. and A. Banerjee, *Short peptide based hydrogels: incorporation of graphene into the hydrogel*. Soft Matter, 2011. **7**(19): p. 9259-9266.
71. Park, S., et al., *Graphene oxide papers modified by divalent ions—enhancing mechanical properties via chemical cross-linking*. ACS nano, 2008. **2**(3): p. 572-578.
72. Worsley, M.A., et al., *Synthesis of graphene aerogel with high electrical conductivity*. Journal of the American Chemical Society, 2010. **132**(40): p. 14067-14069.
73. Tien, H.N., et al., *Synthesis of a highly conductive and large surface area graphene oxide hydrogel and its use in a supercapacitor*. Journal of Materials Chemistry A, 2013. **1**(2): p. 208-211.
74. Cong, H.-P., P. Wang, and S.-H. Yu, *Stretchable and self-healing graphene oxide–polymer composite hydrogels: a dual-network design*. Chemistry of Materials, 2013. **25**(16): p. 3357-3362.
75. Worsley, M.A., et al., *High surface area, sp<sup>2</sup>-cross-linked three-dimensional graphene monoliths*. The journal of physical chemistry letters, 2011. **2**(8): p. 921-925.

76. Novoselov, K.S., et al., *A roadmap for graphene*. Nature, 2012. **490**(7419): p. 192-200.
77. Sun, H., Z. Xu, and C. Gao, *Multifunctional, ultra-flyweight, synergistically assembled carbon aerogels*. Advanced Materials, 2013. **25**(18): p. 2554-2560.
78. Sui, Z., et al., *Easy and green synthesis of reduced graphite oxide-based hydrogels*. Carbon, 2011. **49**(13): p. 4314-4321.
79. Langmuir, I., *The adsorption of gases on plane surfaces of glass, mica and platinum*. Journal of the American Chemical Society, 1918. **40**(9): p. 1361-1403.
80. Freundlich, H., *Über die Adsorption in Lösungen*. Zeitschrift für physikalische Chemie, 1907. **57**(1): p. 385-470.
81. Redlich, O. and D.L. Peterson, *A useful adsorption isotherm*. Journal of Physical Chemistry, 1959. **63**(6): p. 1024-1024.
82. Brunauer, S., P.H. Emmett, and E. Teller, *Adsorption of gases in multimolecular layers*. Journal of the American Chemical Society, 1938. **60**(2): p. 309-319.
83. Pelekani, C. and V.L. Snoeyink, *Competitive adsorption between atrazine and methylene blue on activated carbon: the importance of pore size distribution*. Carbon, 2000. **38**(10): p. 1423-1436.
84. Allen, S., G. McKay, and J.F. Porter, *Adsorption isotherm models for basic dye adsorption by peat in single and binary component systems*. Journal of Colloid and Interface Science, 2004. **280**(2): p. 322-333.
85. Zhao, H., et al., *Adsorption behavior and mechanism of chloramphenicols, sulfonamides, and non-antibiotic pharmaceuticals on multi-walled carbon nanotubes*. Journal of hazardous materials, 2016. **310**: p. 235-245.
86. Dougherty, D.A., *Cation-pi interactions in chemistry and biology: a new view of benzene, Phe, Tyr, and Trp*. Science, 1996. **271**(5246): p. 163.
87. Cote, L.J., et al., *Tunable assembly of graphene oxide surfactant sheets: wrinkles, overlaps and impacts on thin film properties*. Soft Matter, 2010. **6**(24): p. 6096-6101.
88. Bele, S., V. Samanidou, and E. Deliyanni, *Effect of the reduction degree of graphene oxide on the adsorption of Bisphenol A*. Chemical Engineering Research and Design, 2016. **109**: p. 573-585.

89. Ai, L. and J. Jiang, *Removal of methylene blue from aqueous solution with self-assembled cylindrical graphene–carbon nanotube hybrid*. Chemical Engineering Journal, 2012. **192**: p. 156-163.
90. Gao, Y., et al., *Adsorption and removal of tetracycline antibiotics from aqueous solution by graphene oxide*. Journal of colloid and interface science, 2012. **368**(1): p. 540-546.
91. Yang, S.-T., et al., *Removal of methylene blue from aqueous solution by graphene oxide*. Journal of Colloid and Interface Science, 2011. **359**(1): p. 24-29.
92. Chen, H., B. Gao, and H. Li, *Removal of sulfamethoxazole and ciprofloxacin from aqueous solutions by graphene oxide*. Journal of hazardous materials, 2015. **282**: p. 201-207.
93. Sui, Z., et al., *Green synthesis of carbon nanotube–graphene hybrid aerogels and their use as versatile agents for water purification*. Journal of Materials Chemistry, 2012. **22**(18): p. 8767-8771.
94. Zhao, Z. and E.R. Malinowski, *Window factor analysis of methylene blue in water*. Journal of Chemometrics: A Journal of the Chemometrics Society, 1999. **13**(2): p. 83-94.
95. Bergmann, K. and C. O'konski, *A spectroscopic study of methylene blue monomer, dimer, and complexes with montmorillonite*. The Journal of Physical Chemistry, 1963. **67**(10): p. 2169-2177.
96. Fan, J., et al., *Mechanically strong graphene oxide/sodium alginate/polyacrylamide nanocomposite hydrogel with improved dye adsorption capacity*. Journal of Materials Chemistry A, 2013. **1**(25): p. 7433-7443.
97. Tiwari, J.N., et al., *Reduced graphene oxide-based hydrogels for the efficient capture of dye pollutants from aqueous solutions*. Carbon, 2013. **56**: p. 173-182.
98. Chen, B., et al., *Carbon-based sorbents with three-dimensional architectures for water remediation*. Small, 2015. **11**(27): p. 3319-3336.
99. Liu, F., et al., *Three-dimensional graphene oxide nanostructure for fast and efficient water-soluble dye removal*. ACS Applied Materials & Interfaces, 2012. **4**(2): p. 922-927.
100. Wang, J., et al., *Self-assembly of graphene into three-dimensional structures promoted by natural phenolic acids*. Journal of Materials Chemistry, 2012. **22**(42): p. 22459-22466.
101. De Ridder, D., et al., *Influence of natural organic matter on equilibrium adsorption of neutral and charged pharmaceuticals onto activated carbon*. Water Science & Technology, 2011. **63**(3): p. 416-423.

102. Gao, H., et al., *Mussel-inspired synthesis of polydopamine-functionalized graphene hydrogel as reusable adsorbents for water purification*. ACS Applied Materials & Interfaces, 2013. **5**(2): p. 425-432.
103. Fang, Q. and B. Chen, *Self-assembly of graphene oxide aerogels by layered double hydroxides cross-linking and their application in water purification*. Journal of Materials Chemistry A, 2014. **2**(23): p. 8941-8951.
104. Nardecchia, S., et al., *Three dimensional macroporous architectures and aerogels built of carbon nanotubes and/or graphene: synthesis and applications*. Chemical Society Reviews, 2013. **42**(2): p. 794-830.
105. Wang, Z. and D.E. Giammar, *Tackling Deficiencies in the Presentation and Interpretation of Adsorption Results for New Materials*. Environmental Science & Technology, 2019.
106. Li, J., et al., *Removal of Cu (II) and fulvic acid by graphene oxide nanosheets decorated with Fe<sub>3</sub>O<sub>4</sub> nanoparticles*. ACS Applied Materials & Interfaces, 2012. **4**(9): p. 4991-5000.
107. Yoon, T.H., et al., *Investigation of metal binding sites on soil fulvic acid using Eu (III) luminescence spectroscopy*. Environmental Science & Technology, 1994. **28**(12): p. 2139-2146.
108. Tang, W.-W., et al., *Impact of humic/fulvic acid on the removal of heavy metals from aqueous solutions using nanomaterials: a review*. Science of the Total Environment, 2014. **468**: p. 1014-1027.
109. Lin, D., et al., *Surface-bound humic acid increased Pb<sup>2+</sup> sorption on carbon nanotubes*. Environmental Pollution, 2012. **167**: p. 138-147.
110. Zhao, G., et al., *Few-layered graphene oxide nanosheets as superior sorbents for heavy metal ion pollution management*. Environmental Science & Technology, 2011. **45**(24): p. 10454-10462.
111. Quinlivan, P.A., L. Li, and D.R. Knappe, *Effects of activated carbon characteristics on the simultaneous adsorption of aqueous organic micropollutants and natural organic matter*. Water Research, 2005. **39**(8): p. 1663-1673.
112. Feng, Z., et al., *Biobased Nanographene Oxide Creates Stronger Chitosan Hydrogels with Improved Adsorption Capacity for Trace Pharmaceuticals*. ACS Sustainable Chemistry & Engineering, 2017. **5**(12): p. 11525-11535.
113. Shan, D., et al., *Preparation of porous graphene oxide by chemically intercalating a rigid molecule for enhanced removal of typical pharmaceuticals*. Carbon, 2017. **119**: p. 101-109.

114. Mauter, M.S., et al., *The role of nanotechnology in tackling global water challenges*. Nature Sustainability, 2018. **1**(4): p. 166.
115. Alvarez, P.J., et al., *Emerging opportunities for nanotechnology to enhance water security*. Nature Nanotechnology, 2018. **13**(8): p. 634.
116. Wu, J., et al., *Hierarchical construction of a mechanically stable peptide–graphene oxide hybrid hydrogel for drug delivery and pulsatile triggered release in vivo*. Nanoscale, 2015. **7**(5): p. 1655-1660.
117. Sui, Z., et al., *Green synthesis of carbon nanotube–graphene hybrid aerogels and their use as versatile agents for water purification*. Journal of Materials Chemistry A, 2012. **22**(18): p. 8767-8771.
118. Liu, X.-L., et al., *Preconcentration of chlorophenols in water samples using three-dimensional graphene-based magnetic nanocomposite as absorbent*. Chinese Chemical Letters, 2014. **25**(8): p. 1185-1189.
119. Wang, S., et al., *Adsorptive remediation of environmental pollutants using novel graphene-based nanomaterials*. Chemical Engineering Journal, 2013. **226**: p. 336-347.
120. Li, Y., et al., *Comparative study of methylene blue dye adsorption onto activated carbon, graphene oxide, and carbon nanotubes*. Chemical Engineering Research and Design, 2013. **91**(2): p. 361-368.
121. Apul, O.G., et al., *Adsorption of aromatic organic contaminants by graphene nanosheets: Comparison with carbon nanotubes and activated carbon*. Water Research, 2013. **47**(4): p. 1648-1654.
122. Karanfil, T. and J.E. Kilduff, *Role of granular activated carbon surface chemistry on the adsorption of organic compounds. 1. Priority pollutants*. Environmental Science & Technology, 1999. **33**(18): p. 3217-3224.
123. Tang, C.-Y., et al., *Tannic acid functionalized graphene hydrogel for organic dye adsorption*. Ecotoxicology & Environmental Safety, 2018. **165**: p. 299-306.
124. Leitão, R.C., et al., *The effects of operational and environmental variations on anaerobic wastewater treatment systems: a review*. Bioresource Technology, 2006. **97**(9): p. 1105-1118.
125. Zhang, W., et al., *Fast and considerable adsorption of methylene blue dye onto graphene oxide*. Bulletin of Environmental Contamination and Toxicology, 2011. **87**(1): p. 86.

126. Peng, W., et al., *Adsorption of methylene blue on graphene oxide prepared from amorphous graphite: effects of pH and foreign ions*. Journal of Molecular Liquids, 2016. **221**: p. 82-87.
127. Filina, A., et al., *Antimicrobial hierarchically porous graphene oxide sponges for water treatment*. ACS Applied Bio Materials, 2019.
128. Krupa, N.E. and F.S. Cannon, *GAC: pore structure versus dye adsorption*. Journal-American Water Works Association, 1996. **88**(6): p. 94-108.
129. Lin, X., et al., *Fabrication of highly-aligned, conductive, and strong graphene papers using ultralarge graphene oxide sheets*. ACS Nano, 2012. **6**(12): p. 10708-10719.
130. Yang, D., et al., *Chemical analysis of graphene oxide films after heat and chemical treatments by X-ray photoelectron and Micro-Raman spectroscopy*. Carbon, 2009. **47**(1): p. 145-152.
131. Benaissa, H., *Influence of ionic strength on methylene blue removal by sorption from synthetic aqueous solution using almond peel as a sorbent material: experimental and modelling studies*. Journal of Taibah University for Science, 2010. **4**(1): p. 31-38.
132. Tessmer, C.H., R.D. Vidic, and L.J. Uranowski, *Impact of oxygen-containing surface functional groups on activated carbon adsorption of phenols*. Environmental Science & Technology, 1997. **31**(7): p. 1872-1878.
133. Dreyer, D.R., et al., *The chemistry of graphene oxide*. Chemical Society Reviews, 2010. **39**(1): p. 228-240.
134. Ai, Y., et al., *The effect of pH on the U (VI) sorption on graphene oxide (GO): a theoretical study*. Chemical Engineering Journal, 2018. **343**: p. 460-466.
135. Li, Q., et al., *Pore blockage effect of NOM on atrazine adsorption kinetics of PAC: the roles of PAC pore size distribution and NOM molecular weight*. Water Research, 2003. **37**(20): p. 4863-4872.

## Appendix

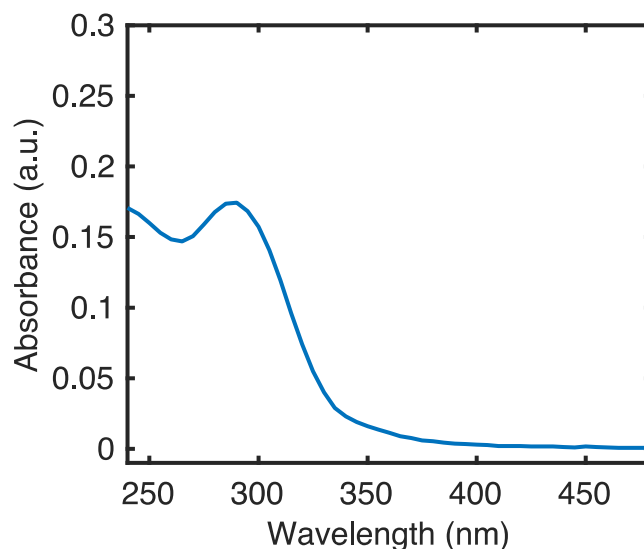


**Figure A1.** Absorption spectrum of the leachate of the rGO-CNC sponge after 24 h of shaking in the experimental set-up at 100 rpm. The absorption peak at 300 nm is characteristic for GO. However, as GO gets reduced during hydrogel formation, the peak should vanish [2]. Strongly reduced rGO does not exhibit the absorption peak at 300 nm. Potentially, the rGO sheets with a lower degree of reduction are not bound to the sponge as strongly as the more strongly reduced sheets, such that they leach out of the sponge over the course of the adsorption experiment. Furthermore, even though the rGO-CNC sponge was thoroughly washed, a remainder of VC (absorption peak at 265 nm) or CNCs (absorption shoulder in the UV-range) might leach from the rGO-CNC sponge in consequence of the mechanical stress during the adsorption experiment.

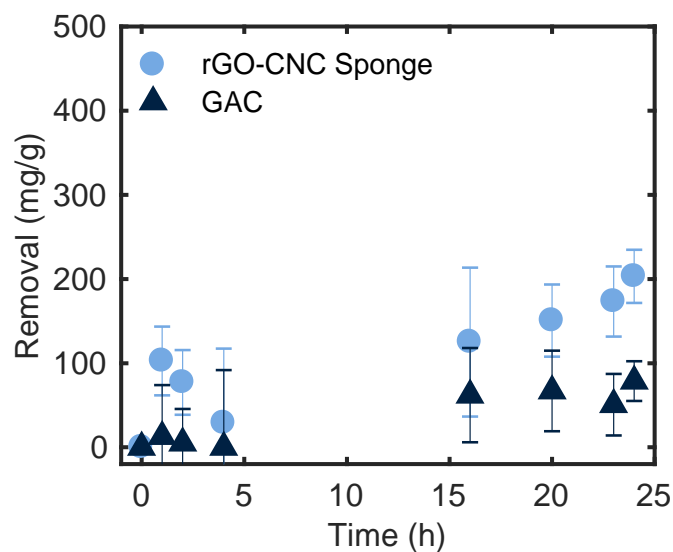


**Figure A2.** Long term kinetics of MB adsorption on the rGO-CNC sponge and on GAC. The initial MB concentration in solution is 30 mg/L, the ionic strength is 0.01 mol/L and the initial pH in solution is 6. As the MB removal on both adsorbents levels out after 16 h, the equilibrium removal was approximated as the MB removal after 24 h.

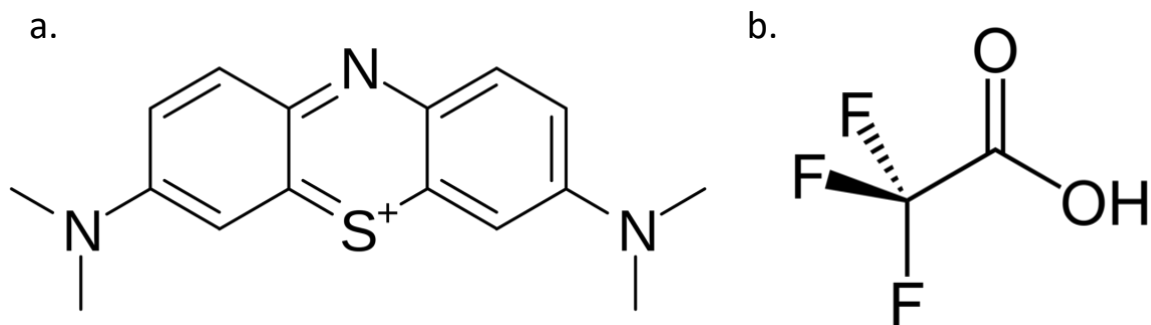


**Figure A3.** Molecular Structure of (a) Methylene Blue and (b) Trifluoroacetic Acid.

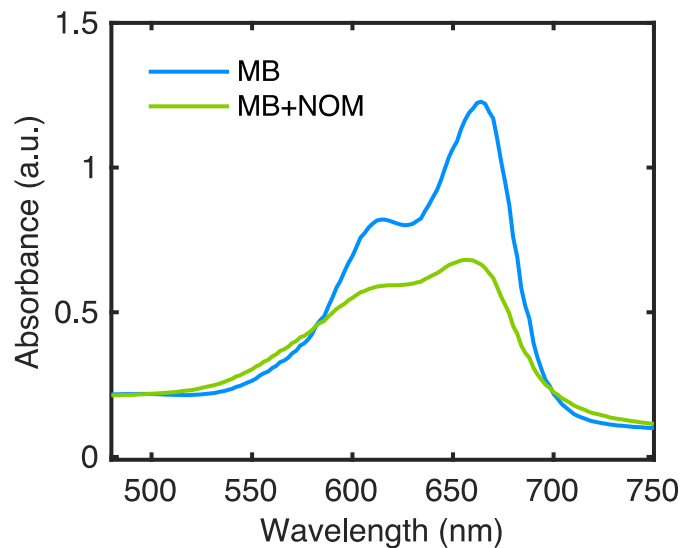


**Figure A4.** Characteristic absorption spectra of pure MB solutions and solutions that contain both MB and NOM.

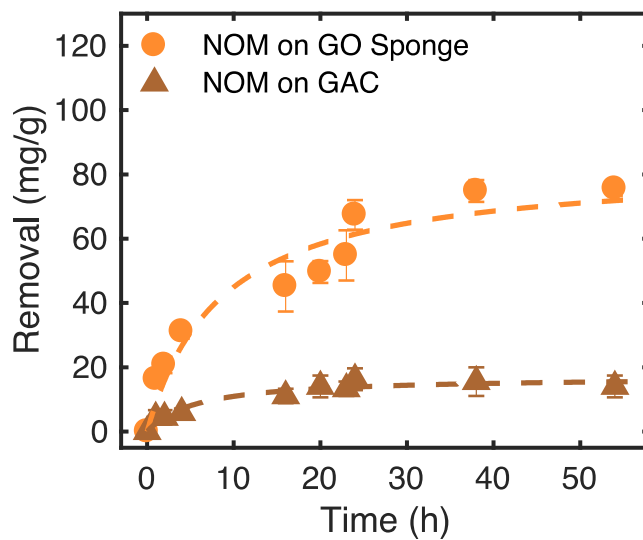


**Figure A5.** Long term kinetics of NOM adsorption on the rGO-CNC sponge and on GAC. The initial NOM concentration in solution is 10 mg/L, the ionic strength is 0.01 mol/L and the initial pH in solution is 6.

